PROCEEDINGS A

royalsocietypublishing.org/journal/rspa

Research

Cite this article: Freissler R, Schuberth BSA, Stotz IL, Zaroli C. 2026 Towards integrating tomographic resolution and uncertainty information into geodynamic mantle flow reconstructions. *Proc. R. Soc. A* **482**: 20250670.
https://doi.org/10.1098/rspa.2025.0670

Received: 30 July 2025
Accepted: 17 November 2025

Subject Areas:
geophysics

Keywords:
finite-frequency seismic tomography, global geodynamics, dynamic topography, mantle flow reconstruction, geodynamic adjoint method, SOLA Backus–Gilbert, tomographic uncertainty, tomographic resolution

Author for correspondence:
R. Freissler
e-mail: roman.freissler@lmu.de

One contribution to a special feature 'Foundations of Operational Geodynamics' organized by guest editors Hans-Peter Bunge, Huw Davies and Sergei Lebedev.

Electronic supplementary material is available online at https://doi.org/10.6084/m9.figshare.c.8203613.

THE ROYAL SOCIETY
PUBLISHING

Towards integrating tomographic resolution and uncertainty information into geodynamic mantle flow reconstructions

R. Freissler[1], B. S. A. Schuberth[1], I. L. Stotz[1] and C. Zaroli[2]

[1]Department of Earth and Environmental Sciences, Geophysics, Ludwig-Maximilians-Universität München, Theresienstr. 41, München 80333, Germany
[2]Institut Terre et Environnement de Strasbourg, UMR 7063, Université de Strasbourg, EOST/CNRS, Strasbourg CEDEX 67084, France

RF, 0009-0002-5073-3571; BSAS, 0000-0002-2706-1589;
ILS, 0000-0002-0760-8276; CZ, 0000-0001-7835-8529

For reconstructing mantle flow back in geologic time, geodynamic inversions require input from seismology in the form of tomographic images. However, a practical representation of image uncertainty is needed for robust inferences. Addressing the scale discrepancy between fluid dynamic predictions and seismically visible heterogeneity is crucial, since the subsequent validation of mantle flow trajectories involves surface dynamic topography predictions that are highly sensitive to the tomographic input. Here, we conduct a synthetic experiment to illustrate the challenges in quantitatively integrating tomographic and geodynamic models, using a linear tomographic framework, the subtractive optimally localized averages (SOLA) method and a mantle circulation model (MCM) as reference. We propose a possible workflow for adjoint flow reconstructions that aims to leverage the capabilities of the SOLA method. This includes the construction of tomographic averaging kernels that can be spatially optimized and which define local resolution, together with model averages and their uncertainties. For the geodynamic adjoint framework, we suggest incorporating the SOLA estimates in the cost function and testing the implementation of specific tomographic realizations in closed-loop experiments. We stress that only after accounting for the effects of resolution, an ensemble approach for uncertainty quantification can provide meaningful constraints on the flow history.

1. Introduction

Convection in Earth's mantle is the fundamental process that controls the geologic history of our planet. Obtaining tighter constraints on its exact evolution and on the feedbacks of different geophysical and geological phenomena, however, is still a formidable challenge. Theoretical time-dependent flow models are in this regard pivotal for addressing long-standing geoscientific problems such as the dynamic description of plate tectonics [1] and lithospheric stresses [2], the interpretation of long-term variations in the global sea level [3] and the coupled evolution of the core-mantle system [4], to name but a few. A major step in this direction has been the development of global mantle circulation models (MCMs) in the last 30–40 years [5–9]. By solving the conservation equations of mass, momentum and energy in a three-dimensional (3D) spherical shell, MCMs provide independent predictions of density variations and convective forces in the mantle (e.g. [10,11]). Observational constraints are explicitly incorporated in the MCMs through the assimilation of horizontal plate velocities from global tectonic reconstructions (e.g. [12–15]). Providing this surface boundary information is critical to obtain correct locations and realistic morphologies of subducting slabs in the flow model. The associated flow histories generate distinct expressions of mantle heterogeneity that mirror the hypotheses encompassed by an MCM. It is possible to test them through geophysical predictions made directly from the flow model. For the present-day state, these include seismic traveltimes [16–18] and anisotropy [19–21], as well as geoid undulations [22]. Furthermore, the time trajectory of modelled mantle flow is reflected in large-scale uplift and subsidence of the surface, computed as so-called dynamic topography [23], as well as in the distribution of geochemical tracers [24].

Critical aspects of the geodynamic forward simulations of convection are the choice of Earth-like flow parameters and the initial condition in the past. The problem of the principally unknown initial condition, however, can be formally dealt with by reconstructing mantle flow backwards in time. For this objective, an inverse modelling approach is needed. A mathematically profound technique for this is nowadays available through geodynamic inversions based on the adjoint method [25–33]. The goal of this iterative framework is to reconstruct past mantle flow states based on the forward model describing the time-dependent convection process and the mantle's present-day state derived from global seismic tomography. This type of inference is also called ‘retrodiction‘ [31]. Its application to the mantle flow restoration problem provides plenty of opportunities to intimately connect several lines of deep Earth research across geology, geochemistry, geodesy, mineral physics and seismology [34]. Assuming that the input information from plate reconstructions, mantle rheology as well as seismic tomography are accurately known, it has been suggested by theoretical studies that mantle flow can successfully be reconstructed back to approximately 100 Ma [35–37] or about one mantle transit time.

To drive the flow reconstructions, a direct misfit between tomographic image and geodynamic forward model is evaluated in each adjoint iteration and minimized in a cost function. A principal challenge in this comparison of geodynamic model and seismic observations is the length-scale discrepancy between simulated and imaged mantle heterogeneity. Structural variations in geodynamic models at Earth-like convective vigour occur on much smaller scales and with sharper amplitude contrasts than can be resolved in tomographic images [38]. In figure 1, we give a visual impression of how the patterns and amplitudes for shear-wave velocity structure may differ between an MCM and actual tomography of the mantle [39]. Furthermore, one needs to consider that tomographic images are the result of inverse modelling. Inhomogeneous data coverage and model errors make them subject to non-uniqueness that requires regularization,

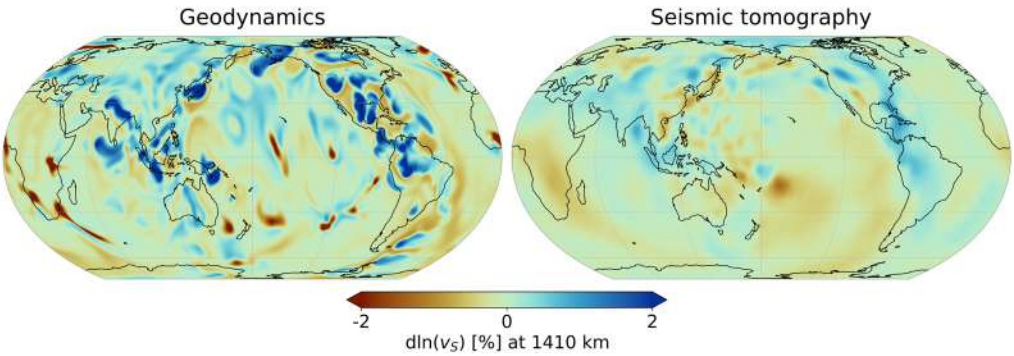

Figure 1. Depth slices at 1410 km showing the shear-wave velocity structures of an MCM (left) and a tomographic model derived from real seismic observations (right). The tomographic model (from [39]) is based on SOLA Backus–Gilbert finite-frequency tomography. Details of the geodynamic model and on the conversion of temperatures to seismic velocity, are given in the electronic supplementary material.

with important consequences for geodynamic inverse models. The fact that seismic images provide only a blurred and non-unique representation of the actual structure at depth raises a fundamental question on the effectiveness of the geodynamic adjoint approach [37]: to what extent is our ability to reconstruct the flow evolution in time affected by the overall tomographic uncertainty? It has been demonstrated that the recovered flow trajectories are indeed strongly influenced by the chosen tomographic reference state [33,37]. Therefore, it is vital to develop a quantitative understanding of the impact of seismic data errors and how information on tomographic resolution and model uncertainty inherent in the imaging process can formally be incorporated in the workflow of geodynamic retrodictions.

In this contribution, we discuss the challenges of using seismic tomography as input in geodynamic adjoint reconstructions of past mantle flow. Our goals are to illustrate the immanent difficulties encountered in this endeavour and to develop ideas for dealing with the effects of limited tomographic resolution and seismic data uncertainty in future. To this end, we conduct a completely synthetic tomographic experiment in a 3D geodynamic mantle flow model using the subtractive optimally localized averages (SOLA) Backus–Gilbert tomographic framework [39–41]. Essential for our purpose, the SOLA method not only provides tomographic images but allows moreover for linking them quantitatively to the mantle structure simulated in the geodynamic models.

In order to bring our ideas for an operational workflow for geodynamic reconstructions into perspective, we first explain in §2a,b the various components of the SOLA-Backus–Gilbert framework, emphasizing its potential to comprehensively characterize the resolution-uncertainty properties associated with a specific seismic inversion. In the uncertainty quantification, data errors that propagate into the tomographic solution play an important role. One contribution to these errors comes from approximate representations of the sensitivity of seismic data to structural variations. We, therefore, provide estimates for these modelling errors by comparing the semi-analytical traveltime predictions used here within SOLA with more accurate measurements from numerical full-waveform seismograms computed in the mantle flow model (§2c). Through these technical steps, we obtain robust tomographic model uncertainties as well as operators for 'tomographic filtering' of geodynamic forward models in a physically consistent and computationally viable form. The filtering replicates the effects of smearing of anomalies and an alteration of heterogeneity amplitudes, which we illustrate for both high- and low-resolution set-ups (§2d). The synthetic seismic imaging of the flow models is crucial to make them comparable to the seismic images and to obtain an accurate and quantitative understanding of the buoyancy distribution from tomography. Finally, in §3, we discuss the potential impact of the different inversion choices in SOLA on mantle flow reconstructions as well as the general limitations when using tomography as geodynamic modelling input. We also provide suggestions for how our description of resolution-uncertainty may be incorporated in the geodynamic adjoint method in future applications through novel cost functions and the design of relevant model ensembles.

2. Tomography in a synthetic mantle

Tomographic imaging requires the following components: seismograms and derived observables (e.g. traveltimes of seismic phases), a forward modelling theory predicting the data in accordance with the nature of the measurement, meaningful representations of data uncertainty and an optimization approach that should produce estimates of model values and potential error metrics for model assessment [42]. We use our experimental set-up based on the MCM to accurately reproduce these steps. The synthetic environment here allows us to illustrate the influence of the individual data and modelling components. This is crucial to understand the general problem of relating tomographic images to actual Earth structure.

To achieve this, we built a complete synthetic seismic data set for the MCM (details on the individual methods and parameter choices, as well as additional depth slices of the MCM can be found in the electronic supplementary material). For modelling mantle flow, we use a standard set of geodynamic parameters (e.g. [10,43–46]) employed in the code *TERRA* [9,10,45,47,48]. The long-wavelength patterns of seismic heterogeneity are in this case also broadly compatible with tomography [38,49,50]. For obtaining seismic velocities, the temperature variations from the MCM are converted to elastic parameters using tabulated values from thermodynamic models of mantle mineralogy, here computed with the software package MMA-EoS [51] together with a correction for the effects of anelasticity [52,53]. Using a modified version of SPECFEM3D_GLOBE [16,54], we then simulated elastic wave propagation in the MCM, accurate down to a shortest period of approximately 10 s, to obtain three-component seismograms for a global data coverage with 3800 earthquakes and 10 000 real and 10 000 virtual station locations (see figure 2). Since in our SOLA tomographic inversions, the focus is on shear-wave velocity perturbations that are modelled with linear finite-frequency kernels (FFKs) [56], we measured cross-correlation traveltime residuals (with the processing of Zaroli *et al.* [57]) from the corresponding 1D-MCM and 3D-MCM seismograms. The measurements overall show great sensitivity to the large-scale structure of the MCM, especially in the lower mantle (figure 2c,d). Earlier traveltimes appear largely owing to fast structures from past subduction dominating around the Pacific, while delayed traveltimes arise from slow structures in the Pacific and under Africa. This underpins theoretical considerations that the first-order contribution to traveltime shifts is accumulated near the ray-turning point. Similar traveltime patterns can also be seen in real data for S-wave traveltime delays (e.g. in [58]), which can be compared to the results for real stations in figure 2c. A more homogeneous data coverage is provided by the virtual stations in figure 2d, which we exploit for quantifying uncertainty in the prediction of the traveltimes (see §2c). Our ‘tomographic data set’ selected for inversion ultimately comprises traveltime residuals only from real station locations. It consists of approximately 200 000 measurements for the phases S, SS, ScS and ScS2, that optimally cover the mantle based on an equidistant ray-turning-point sampling. This has the advantage that correlations in the data should be greatly reduced and we obtain ideal geometries for resolving mantle structure. Although we do this is in a synthetic framework, the use of real stations should allow for a similar set-up also in actual Earth applications. Going beyond body wave traveltimes, many current global tomographies also incorporate information from either surface waves, normal modes or both, which is especially relevant for the imaging upper mantle structure. The use of traveltimes for S phases alone, which have almost vertical incidence angles at seismic stations may, thus, strongly limit the achievable resolution at these depths in our set-up (we show this explicitly in §2b). This is not detrimental to the objectives of the present study. In fact, we propose in §3 how biases from lacking resolution (present to various degrees in all global tomographic inversions) could potentially be dealt with in a geodynamic modelling framework.

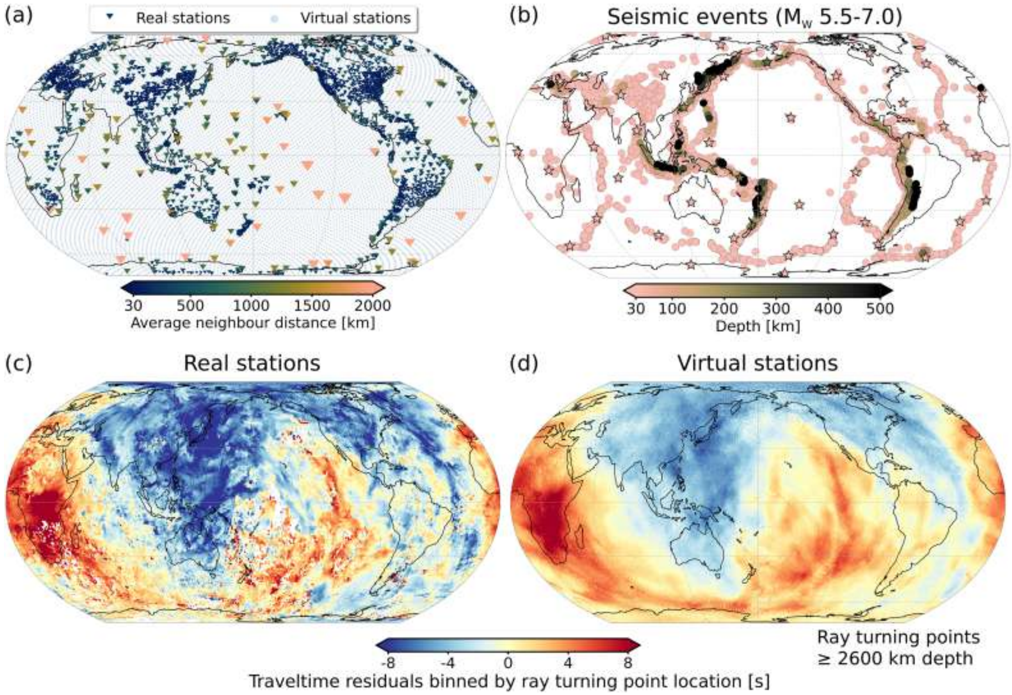

Figure 2. Source–receiver configurations and traveltime residuals for the synthetic tomographic experiment based on an MCM. (a) Geographic locations of the 10 000 real and 10 000 equidistant virtual stations, at which seismograms have been computed numerically. Colour and size of the markers indicate the importance of stations based on their average distance to the nearest neighbouring station. (b) The 3800 seismic events with moment magnitudes M_{W} from 5.5 to 7.0 from the global centroid moment tensor (CMT) catalogue [55], colour-coded by source depth. Stars mark the 50 events that we used for statistical analysis of traveltime residuals to determine the theoretical uncertainty in data prediction (see §2c). (c,d) Cross-correlation traveltime residuals for S and ScS phases turning below 2600 km depth. Specifically, the mean residuals in 1×1 degree cells are shown here, making use of ray turning point locations; for all real (c) and virtual (d) stations.

In general, it is clear that both efforts in improving general seismic data coverage and theoretical progress are necessary to strengthen the link between seismology and geodynamics.

(a) Imaging the mantle with Backus–Gilbert inversion and SOLA

In order to better understand the technical challenge of linking tomographic and geodynamic models, it is instructive to reconsider the original ideas that have led to the formulation of linear inverse theory in geophysics. In a series of papers [59–61], Backus & Gilbert described the inversion process as the problem of finding acceptable model values that explain the data to within their uncertainties. The finite size of data sets and the presence of errors make the results of such an inversion generally non-unique. Backus & Gilbert, however, showed that unique estimates of physical parameters can be obtained by addressing explicitly the limited resolving power of the data. The goal of recovering exact point estimates is, therefore, abandoned in favour of determining localized average values over certain (spatially extended) parameter domains. A global tomographic image can then be constructed by assembling all the model averages, although this is not the main objective in the Backus–Gilbert method. Inversions of this kind are, thus, more suitable for subsequent quantitative interpretations of the parameter values, rather than for seismic data prediction and model building. This targeted approach, focusing on extracting only specific Earth model properties that can be reasonably quantified, has recently gained renewed attention in seismology [39,41,62–66].

One way to formulate Backus–Gilbert inversion is the so-called SOLA method [39,40,67]. Like in the classic Backus–Gilbert method, one directly computes sets of localized averaging kernels, but control on the expected resolution lengths is gained in SOLA through the introduction of freely tunable target kernels of finite size. They may be chosen according to the specific research objective, prior to the actual inversion, to facilitate the construction of useful averaging kernels. The resulting averaging may deviate from the prescribed target function if the data do not permit an exact fit. However, the actual averaging kernels are explicitly known after the inversion and effectively represent the achieved local resolution. Also, a trade-off parameter is included in SOLA that simultaneously moderates the propagation of data errors into the estimated model averages. This means that in SOLA one can opt for either a good fit of the averaging kernels to the target resolution together with larger uncertainties on the model averages or for smaller uncertainties but less well-behaved averaging kernels. This trade-off can be chosen independently for all parameter locations, allowing for a local adaptation to the data coverage (a list of the specific trade-off parameter choices for each figure in this article can be found in the electronic supplementary material). Most important, SOLA makes this quantitative information from the tomographic inversion practically usable.

(b) Averaging/resolving kernels and SOLA model uncertainty

The main advantage of the SOLA method is its ability to compute averaging kernels individually, while having a certain control over resolution lengths and error propagation through inversion parameter choices. In the following, we illustrate how these key features work together and enable a more quantitative linking of tomographic and geodynamic models.

In figure 3, we show the averaging behaviour of our data configuration for two different sizes of SOLA target kernels and for two regions with unequal data coverage. The target locations are both at 465 km depth. Figure 3a shows the two different target kernels at the locations **A** and **B** and their horizontal extent at depth. In order to specify resolution lengths within the target and to assess them after the inversion from the averaging kernels, we employ 3D Gaussian functions. As the corresponding measure of length, we take their horizontal/vertical halfwidths at half maximum (see inner ellipsis, figure 3b). Another useful metric to characterize the quality of averaging kernels is the 'focus' (see [68]). It is a proxy for the robustness of estimated resolution lengths (making use of the outer ellipsis in figure 3b). For details about this concept and the quantification of resolution lengths from global sets of averaging kernels (or other resolving kernels), the reader is referred to Freissler *et al.* [68].

Figure 3c shows the corresponding averaging kernels resulting from the inversion. For location **A**, both inversion set-ups (target resolution lengths of 300/200 km and 500/250 km) show generally a good match to the target. The fit is highlighted with a cyan contour line at the half maximum level of the target kernel, which corresponds to the darkest red isosurface in the averaging kernel. For location **B**, the data coverage is strongly inhomogeneous owing to a sparser distribution of ray paths. Achieving the prescribed target resolution is virtually impossible in this region. Consequently, since we use only body waves for the inversion here, we observe strong vertical smearing (indicated by the dark red area reaching up to the surface) and averaging up to the lithosphere, as well as some kernel side lobes far off the target location. Note that for each target kernel we chose a single trade-off parameter, the second tunable inversion parameter in SOLA. This parameter can be modified to further improve the fit to the target kernel, but at the cost of higher levels of propagated errors. The complexity and large number of averaging kernels for different regions, however, makes it impractical to visually inspect and adapt each of them individually. Also, cross-sections only offer a partial view. Instead, Freissler *et al.* [68] have shown that it is possible to extract resolution lengths in an automated fashion from the averaging kernels using a Gaussian fit as given by the yellow ellipses in figure 3b. To quantify if the derived length estimates from such a fit are actually representative, the aforementioned concept of focus is applied. This way, it can be ensured that only meaningful resolution lengths are used for interpretation. The focus values and estimates of the propagated uncertainty further

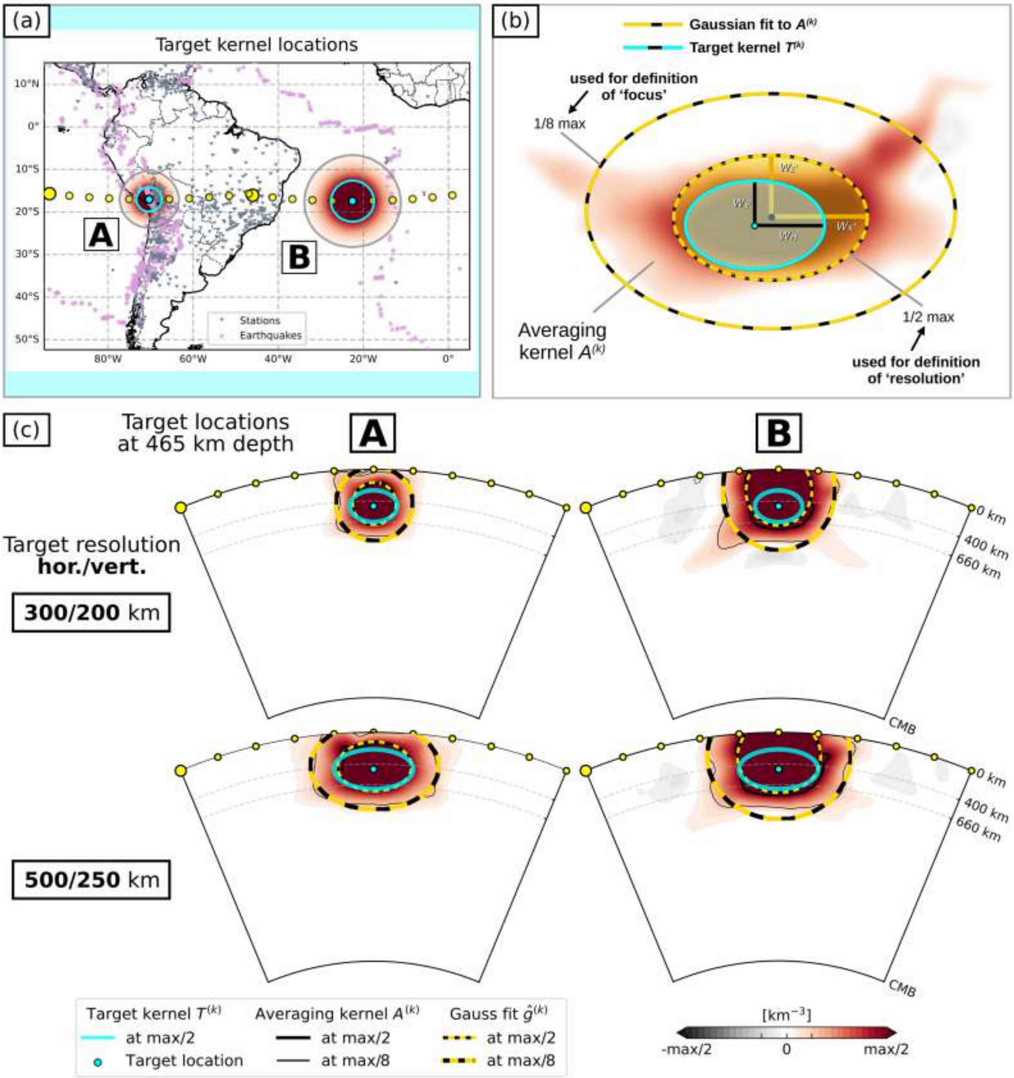

Figure 3. Averaging kernels for two different inversion set-ups: (1) Target kernel with 300 and 200 km horizontal and vertical extent, respectively, together with a trade-off parameter that enforces a strong fitting to the target volume. Target kernels are 3D Gaussian functions and the size is defined here as the horizontal and vertical half widths at half maximum, (2) a target kernel with half widths of 500/250 km and a different trade-off parameter choice with less emphasis on target fitting but correspondingly lower propagated uncertainty. (a) Target location A with good and B with poor data coverage. (b) Concept for determining resolution lengths and their robustness with 3D Gaussian estimates and the 'focus' ellipsoid (see [68]). (c) Vertical west-east cross-sections of different averaging kernels, with ellipses representing length scales of the target resolution (cyan), the estimated *a posteriori* resolution (inner gold-dashed) and the focus region (outer gold-dashed).

provide guidance in which way the target resolution and error levels need to be adjusted to serve a specific research purpose [68].

As it is possible with SOLA to estimate resolution lengths for an entire global set of tomographic model parameters, they can be explored in more detail all together by combining them on a map (figure 4). The maps at a depth of 735 km reveal that there is a good control on the horizontal resolution for the given target lengths of 300 and 500 km, while vertical resolution strongly deviates from the target of 200 and 250 km. Especially, in the Pacific, there are notably large resolution lengths exposing a gap in the data coverage. A benefit of the SOLA

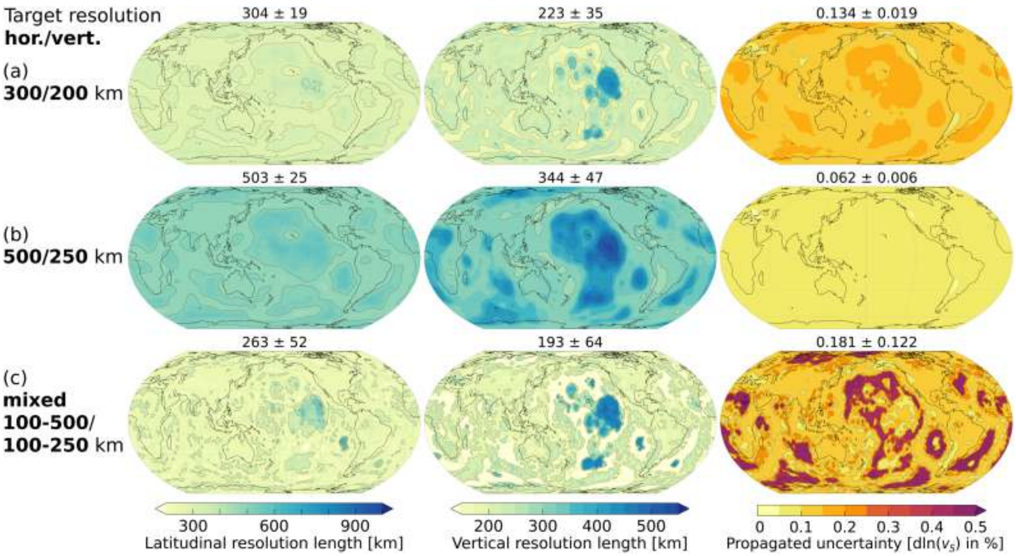

Figure 4. Global maps of latitudinal (i.e. horizontal in the N-S direction) and vertical resolution lengths, as well as propagated model uncertainty at a depth of 735 km for different inversion parameter combinations: (a) target kernels with 300/200 km half width size and constant trade-off parameter, (b) target kernels with 500/250 km size and constant trade-off parameter and (c) variable target kernel sizes and trade-off parameters combined in one model representation, where the focus value, as defined in [68], is closest to 1. A value of 1 is indicative that the interpretation of resolution lengths with a 3D Gaussian function is valid. Values above each map give the global mean ± s.d. of all estimates.

method is that for each parameter location, an individual choice of inversion parameters—target kernel size and trade-off parameter—can be made, while still resulting in a single model. We, therefore, performed several inversions, varying the target resolution length horizontally from 100 to 500 km and vertically from 100 to 250 km. The final combination is chosen according to the best focus value obtained and shown in the bottom row of figure 4. One can see at the same time in the right-hand column of figure 4 that for narrower averaging kernels, errors in the data propagate more strongly into the estimated model averages. For averaging kernels with around 200/100 km extent present in the mixed map, model uncertainties may reach deviations of the shear-velocity perturbation of over 0.5%, rendering a direct dynamic interpretation of the imaged seismic velocities problematic. For more details on SOLA tomography and the impact of different inversion parameter choices, the reader is referred to Freissler *et al.* [68]. Note again that apart from the inversion parameters that we described here, the earthquake-station configurations and estimates of data uncertainty play a crucial role in defining the properties of the resulting model.

(c) Seismic data prediction and associated errors

The SOLA inverse operator (i.e. the matrix with Backus–Gilbert coefficients) allows for a direct propagation of data errors, which can be used to analyse uncertainties in the estimated model averages [39,40,67]. This means that data uncertainties need to be carefully estimated for the model uncertainties to be informative. While the error from measuring seismic signals is commonly acknowledged and estimated (e.g. [57,69]), one aspect that has received only minimal attention in tomography is the accuracy of data prediction. In our case, the data consist of cross-correlation traveltime shifts measured at 22.5 s centre period and for computing the data sensitivities, we use the appropriate paraxial FFKs (also called *banana-doughnut kernels* see [56,70]). They relate S-wave traveltime residuals to velocity variations in the model. These linear kernels involve a number of approximations that potentially limit their accuracy in the presence of complex mantle heterogeneity [56,71]. The associated errors have so far not been taken into account in global tomographic inversions and forward modelling tests have typically been performed in seismic models that are much smoother than the velocity fields predicted from a high-resolution geodynamic model (e.g. [58,72,73]).

Therefore, to quantify the errors in synthesizing traveltimes, we compare the FFK predictions of the different phases against cross-correlation measurements using full-waveform synthetic seismograms computed by numerically solving the 3D wave equation in the MCM. In taking the MCM as a reference, we assume that the errors in computing the synthetic seismograms and of the cross-correlation measurements are negligible compared to the inaccuracies of the FFK predictions. To obtain spatially unbiased statistics, we only consider the 10 000 virtual stations and the set of 50 equidistant earthquakes here, both shown in figure 2a,b. Details on the simulations and measurements can be found in the electronic supplementary material. The results in figure 5 reveal the deviations of all FFK predictions from the cross-correlation measurements. The strongest discrepancies can be seen for SS and the ScS2 phase, that both experience a surface reflection and are preferentially recorded at epicentral distances greater than 60°. Root-mean-square (RMS) errors are between 0.62 and 4.06 s for the different phases (see table 1). In total, the differences can be explained by unmodelled 3D wave effects or an inadequacy of a given FFK. But also some stronger outliers may indicate that in fact also the reference cross-correlation traveltimes might suffer from relevant measurement errors, for instance, through poor time window selection. In addition to the data prediction error, further factors contribute to the complete uncertainty in the inversions: source mislocation and independent random measurement errors that we consider here as well. The mean values of the final data uncertainties range between 2.58 and 4.84 s; also listed in table 1. While these are arguably conservative estimates, our results suggest that the theoretical errors from data prediction are not negligible for realistic mantle heterogeneity, especially for complex phases like ScS2. The magnitudes of these errors also become increasingly more relevant the finer the structure we intend to resolve, so that an underestimation could lead to an inaccurate representation of the actual resolving capabilities.

(d) Tomographic filtering

As an important processing step for the quantitative comparison of geodynamic models to tomographic images, the former need to be tomographically filtered as outlined in §1. To this end, one can either use the resolution operator $\mathcal{R}$ (where the rows can be seen as the individual averaging kernels) [38,75–78] or use the generalized inverse projection (GIP) [79]. The GIP method has the advantage that it allows for data error propagation. Tomographic filtering provides a consistent comparison of the geodynamic and seismic Earth model because it is based on a linear mapping that does not depend on the underlying data values themselves. In the GIP approach, one simply takes the generalized inverse of a Backus–Gilbert-type inversion to project a data vector to model space. Conceptually, this is equivalent to using the classic approach with the resolution operator, which, however, requires an unphysical reparameterization of the original MCM to conform with the underlying tomographic grid. We, therefore, make use here of the GIP approach and the cross-correlation measurements from the synthetic MCM seismograms. Since we factored in the prediction errors in the total data uncertainties (see §2c), FFK predictions would be a valid choice as well. In the case of real tomography, one would use actual Earth observations instead and the resulting image then represents a reference for the filtered MCM.

In general, filtering leads to a distortion of seismic anomalies through blurring and alteration of amplitudes of seismic heterogeneity. These effects are to varying degree present in all tomographies as a consequence of the underdetermined nature of the associated inverse problem. Notably, this makes the outcomes of filtering also dependent on the specific choices for the inversion parameters. In figure 6, we demonstrate how the different values for the target resolution in SOLA (shown in figure 4) lead to changes in the tomographically filtered representation of the original MCM. As expected, narrower averaging kernels lead to imaged structures that better resemble the unfiltered MCM, especially in terms of amplitudes around

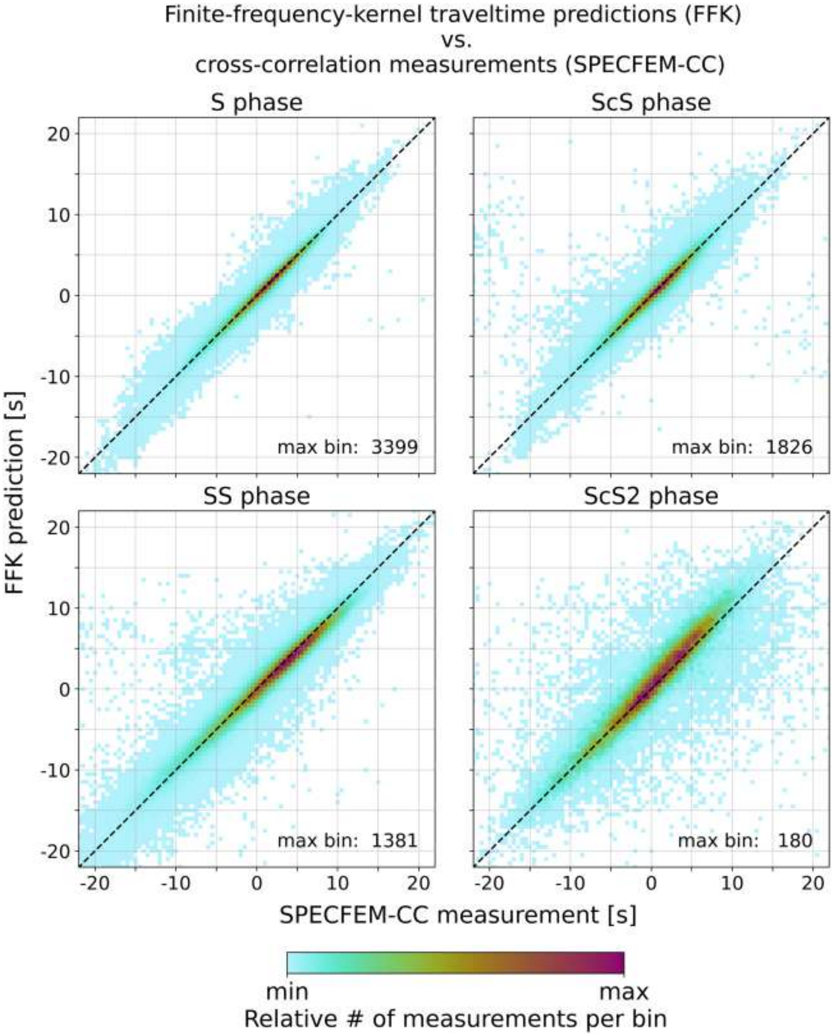

Figure 5. Traveltime predictions using FFKs [56,74] versus cross-correlation measurements using synthetic seismograms from SPECFEM3D_GLOBE [54] ('SPECFEM-CC'). Both data sets were generated for the 3D seismic structure of the MCM. Comparisons are shown for the seismic phases S, SS, ScS and ScS2. The traveltime residuals are binned by 0.5 s intervals and they are coloured relative to the maximum bin count achieved for a given phase. The relative minimum corresponds to bins with only a single valid measurement. The dataset includes measurements from a reduced set of source–receiver configurations, with 50 equidistant earthquakes and 10 000 virtual stations (see also figure 2).

Table 1. Seismic phases and estimates of data prediction errors σ_{pred} as well as the mean of the final data uncertainties $\bar{\sigma}_d$ used in the synthetic SOLA tomographic inversions.

phase	no. measurements	prediction error σ_{pred} (s)	mean data uncertainty $\bar{\sigma}_d$ (s)
S	118 400	0.62	2.58
ScS	10 800	1.87	3.12
SS	60 000	1.98	3.25
ScS2	10 800	4.06	4.84

the most prominent slabs and plumes. However, there are some relevant observations that would need to be considered for dynamic interpretations. First, there is still a substantial difference between filtered and original structure, even for our idealized synthetic inversion

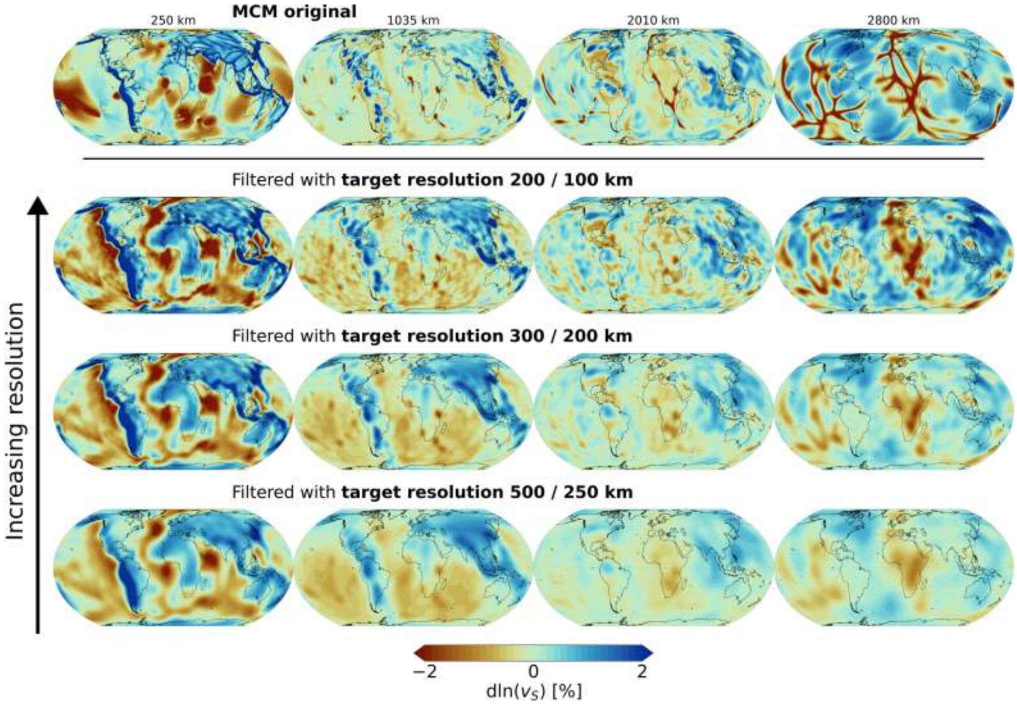

Figure 6. Comparison of the original MCM (top row) and tomographically filtered representations that employ different target resolution lengths (with horizontal/vertical extents of 200/100, 300/200 and 500/250 km, respectively; second to bottom row). The filtered models are the result of applying the GIP [79] to the synthetic tomographic data set consisting of 200 000 cross-correlation traveltime residuals generated for the MCM. The cross-correlation measurements were performed on SPECFEM3D_GLOBE seismograms for real source-receiver configurations. The depth slices are at 250, 1035, 2010 and 2800 km that correspond to the midpoints of tomographic layers in the radial parameterization.

set-up. This can most clearly be seen for the upper mantle at 250 km depth (figure 6, first column), but also in better resolved regions like Europe at 1035 km depth (figure 6, second column). There, a distinct cold downwelling is damped and smeared across the continent. Second, another general observation is the occurrence of conspicuous small-scale anomalies, especially for the high-resolution set-up using 200/100 km target kernels. Often these seem to not be directly related to any specific anomaly and they appear in extended regions of 'normal mantle' (i.e. regions at 0% velocity perturbation in the original, unfiltered model). For example, across the oceans at 1035 km depth, additional slow anomalies occur after tomographic filtering in the proximity of plumes, probably as a consequence of horizontal and vertical smearing of transition zone heterogeneity. Finally, looking at the lowermost mantle, an intriguing observation after applying the tomographic filter is the morphological and amplitude change of the hot filament-like structures that are characteristic for thermal convection. If these filaments are located close enough to each other, it is possible that the impression of a pile structure may arise, merely from the tomographic imaging process (see also [80]).

Tomographic data uncertainties further complicate these comparisons. By extrapolation, one could naively assume that by increasing the resolution with suitable SOLA inversion parameter choices e delta-like target resolution kernels, it would be possible to recover the 'true' structure (see top row figure 6), which is, however, not the case. There is a lower bound to the resolving capability set by the size and structure of the data sensitivity kernels with their corresponding Fresnel zones, which are controlled by the frequency content of the seismic measurement. Another limiting factor is also the grid spacing in the discretization of the tomographic model. So, instead of accurately recovering the original MCM, there would be a substantial increase in propagated uncertainty, as can be seen in figure 4, plus a degradation of the averaging kernels through increased side lobes and high-amplitude oscillations on short scales, which tend to produce strong artificial velocity variations. This may render such a 'high-resolution' tomographic model unusable.

Summarizing the control on tomographic model properties, there are three scenarios that we can explicitly produce with SOLA: (1) a high-resolution and high-uncertainty case, which could theoretically capture all dynamically relevant length scales, but may at the same time suffer from strong errors in model average estimates; (2) a low-resolution low-uncertainty case, with little control on the recovery of small features, but high confidence in the values of the large-scale structure and (3) a mixed case with possible local tendency towards one or the other end-member scenario. In general, different SOLA inversion parameter choices can be equally valid for filtering, as long as the complete model information is taken into account in subsequent interpretations and inferences. In particular, resolution lengths are critical to robustly account for the scale discrepancy of geodynamic and tomographic models, as we further detail in the following section.

3. Implications for mantle flow reconstructions

In the previous sections, we have illustrated that with SOLA, one can not only build a tomographic model but also obtain the full information about resolving length scales and propagated errors and how they correlate. This allows us to construct tomographic models and the associated filtering applications in a consistent manner. Moreover, model and filtering operators can together be tuned towards specific geodynamic purposes.

Direct control on tomographic resolution and uncertainty is especially relevant for geodynamic inverse models of mantle flow that make use of the adjoint method, in which tomographic images are an explicit input. It is obvious that through the imperfect imaging process and the tomographic-geodynamic length-scale discrepancy, the resulting flow trajectories may mismatch the actual flow evolution in real Earth, even if all other parameters were robustly known. In turn, if the influence of tomographic uncertainty could be better understood, this would allow for an improved control on the other two critical, but also uncertain retrodiction components, namely, rheology and the assimilated horizontal plate motions [37].

We discuss in the following, in what way the reconstruction of mantle flow and its appraisal could be affected by the specific choice of a tomographic model and its associated resolution and uncertainty. In particular, we make some suggestions on how the seismic information concerning resolution lengths and error propagation can technically be incorporated in the general workflow of geodynamic inversions.

(a) Tomographic cost function for geodynamics

In its simplest formulation, the geodynamic adjoint method (as defined in [30]) can be described as finding an optimum temperature initial state $T(\mathbf{r}, t_0)$ in the geologic past as a solution to

$$\min_{T(\mathbf{r},t_0)} \frac{1}{2} \int_V \int_{t_0}^{t_{\text{now}}} (T(\mathbf{r},t) - T^{\text{tomo}}(\mathbf{r}))^2 \delta(t - t_{\text{now}})\, \mathrm{d}t\, d^3\mathbf{r}, \tag{3.1}$$

subject to the conservation equations governing mantle flow and its time evolution over $t \in [t_0, t_{\text{now}}]$. At a practical level, in the adjoint framework one starts by running a geodynamic model forward in time until present-day (i.e. we compute a standard MCM). At this final state, as indicated by the delta function in equation (3.1), the geodynamic model $T(\mathbf{r}, t)$ and the reference temperature state derived from tomography $T^{\text{tomo}}(\mathbf{r})$ are compared in the entire spatial model domain (at all points $\mathbf{r} \in V$), making use of a specifically chosen misfit or cost function. In the example here, an ordinary least-squares misfit is used. After the first geodynamic forward model run, we are usually faced with large differences between $T(\mathbf{r}, t_{\text{now}})$ and $T^{\text{tomo}}(\mathbf{r})$; visually this can be seen again in figure 1. Adjoint equations then allow us to determine how the initial condition of the geodynamic model $T(\mathbf{r}, t_0)$ has to be updated. The objective in the cost function is, thus, to reduce the difference of the geodynamic and tomographic temperature states in the subsequent forward model run. Updates to the initial condition are then iteratively determined and we can achieve a reconstruction of flow that is theoretically consistent with the observed mantle state at present-day.

The use of a cost function in the form of equation (3.1), however, implies that we would know how to perfectly derive $T^{\text{tomo}}(\mathbf{r})$ from the tomographically estimated seismic velocities. One challenge, that we do not address here, lies in the potential presence of chemical heterogeneity. The effects of compositional variations can be incorporated in adjoint calculations [81], but they are difficult to isolate, in particular, owing to the dominant role of thermal variations on seismic anomalies [82]. Together with the depth- and temperature-dependent stability fields of mineral phases, this hinders unique conversions from seismic velocities to temperature. A second complication arises from seismic resolution and filtered model amplitudes, as elaborated throughout this paper. Systematic deviations in the retrieval of temperatures are consequently expected, especially near phase transitions. The interplay of resolution and nonlinear (compositional-) mineralogical mapping has been shown to introduce global depth-dependent averaged errors of up to approximately 200 K at the current state of knowledge [83] (disregarding additional uncertainty from mineral physics laboratory measurements, anelasticity corrections, chemical composition, water/melt content, etc.). There is, thus, an input uncertainty in geodynamic adjoints associated with $T^{\text{tomo}}(\mathbf{r}, t_{\text{now}})$ that should be reflected in any application of the method. This necessitates modifications of the cost function to account for biases, in our case the ones from tomographic resolution and to prevent overfitting in the presence of errors [30].

Previous attempts to accomplish this have used the spherical harmonics misfits [33,36], or radial damping and gradient smoothing have been proposed [84], neither of which directly account for the mostly heterogeneous resolution in tomography. Still, the principal idea that has been pursued is the following: large-scale buoyancy forces are the primary drivers of convection and, thus, discrepancies in smaller length scales of heterogeneity should carry less significance in the adjoint misfit and should not inhibit model convergence [37]. The misfit reduction should, however, also focus at best on the length scales and uncertainty ranges that are actually robustly imaged in the tomographic model. As a result of using cost functions that account for this, the modelled flow may still freely develop thermal anomalies on smaller length scales dictated by the dynamics, while still fitting tomography. For a fully operational application of the geodynamic adjoint method, other Earth observations and their integration in the cost function also remain important [33]. They may also appear as additional regularization choices in the cost function (e.g. [84,85]) and contribute as well to tying reconstructed flow trajectories closer to the true evolution. In the following paragraphs we discuss, with examples from our synthetic tomographic experiment, in what way specifically the cost function and its adaptation to the tomographic situation is crucial for improving geodynamic retrodiction models.

(b) Mismatch in heterogeneity amplitudes

RMS values of seismic velocity variations are a traditional quantitative measure to compare tomography and geodynamic models (e.g. [10,49]). They can be seen as the depth-dependent average deviation of the 3D velocity structure from the normal mantle. Therefore, the RMS amplitudes are a good indicator for the integrated strength of seismic anomalies and, thus, variations in total buoyancy, which characterizes the dynamic relevance of different mantle regions. The tomographic filter effect can have a significant impact on the interpretation of RMS values [38]. In figure 7, we plot whole-mantle RMS profiles for the original MCM and for the correspondingly filtered models (see also figure 6). To determine the influence of resolution, it is informative to show these profiles together with the resolution estimates from the underlying SOLA averaging kernels. We notice that especially the average vertical resolution is linked to mismatches in the RMS values. Larger-sized averaging kernels in general reduce

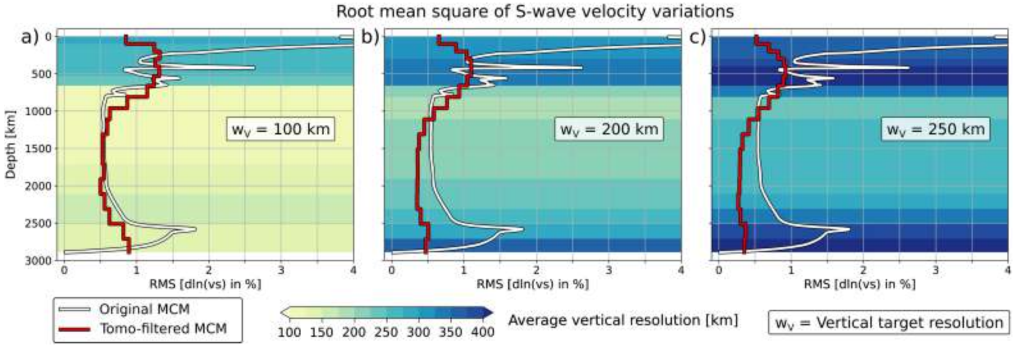

Figure 7. RMS profiles of the shear-wave heterogeneity for the original MCM (white lines) and for the filtered representations (red lines) with different vertical target resolution lengths of (a) 100, (b) 200 and (c) 250 km. In the background, the globally averaged vertical resolution lengths estimated from SOLA at specific depth intervals are plotted. Owing to the use of body waves restricted to epicentral distances greater than 30° and the fact that we use the phases S, SS, ScS and ScS2 only, vertical resolution is severely limited in the upper 600 km and may differ by as much as approximately 200 km from the target length.

the recovered RMS amplitudes, as expected. For the upper mantle and transition zone, there is a substantial mismatch between the profiles of the filtered and the original MCM, related to vertical smearing. The kernels at this depth average over the heterogeneity from phase transitions and from the uppermost layer in the MCMs, which both feature strong velocity amplitudes. This markedly increases the filtered RMS relative to the original profile, particularly directly below the transition zone. Directly at the phase transitions, however, filtered models do not show any significant RMS peak as present in the original MCM. Correctly capturing these amplitudes in the mantle transition zone would probably require resolving the structure on length scales of approximately 50 km vertically and less. This theoretical estimate can be deduced from the magnitude of expected topographic undulations around the major seismic discontinuities [86]. Another occurrence of the vertical averaging effect is observed in the lowermost mantle where bridgmanite transforms to post-perovskite [87], which is also associated with high RMS amplitudes. For a vertical target length of 100 km (figure 7a), the resulting vertical resolution of approximately 150 km in the deepest mantle lead again to a discernible peak in the filtered RMS curve. But, the RMS amplitudes differ by as much as approximately 1% at 2550 km depth and the filtered MCM does not feature a sharp change from high, back to lower RMS values. Such effects could lead to invalid interpretations of tomography, suggesting a much deeper occurrence of post-perovskite and, therefore, a misrepresentation of its dynamic effects. Only at depths of approximately 1000–2500 km, that is, away from the major phase transitions, is the resolution of the SOLA inversions with the 200/100 km target kernels adequate for capturing the shape of the original RMS curve. This indicates that the local dynamic effects of phase transitions cannot be fully captured in the adjoint flow reconstructions by means of data assimilation of global tomography alone. Robl *et al.* [83] came to a similar conclusion, analysing the effects of resolution on the recovery of seismic velocities with other published tomographic filters. They conclude that using approximative mineralogical mappings for the conversion from tomographically imaged seismic velocities to temperatures might be a better choice than using the full thermodynamic mineralogical tables. This partially mitigates the errors associated with phase transitions, particularly when lower-resolution tomographies are considered.

(c) Length scales of heterogeneity and relation to dynamic topography

The maps of the filtered MCM structure in figure 6 and the RMS curves in figure 7 suggest that key information for geodynamic modelling lies in the resolution lengths. They effectively indicate the regions where major deviations of tomography from the actual structure can be expected and where significant mismatches in the imaged and actual buoyancy may appear. Evidently, this has profound implications for subsequent predictions derived from a tomographic state estimate of the mantle. This is in particular not only true for the inferred present-day dynamic topography, but also its variations over time. To make this aspect more graspable, we take a tomographic perspective on this surface observable in the context of flow reconstructions in the following. For a deeper discussion on the geodynamic relevance and interpretation of dynamic topography, the reader is referred to [23,88–91].

Dynamic topography is essentially the vertical response of the surface (or the CMB, which we do not further consider here) to density variations and the associated stresses in the mantle. In flow reconstructions, the retrodicted mantle trajectory translates into a time-varying surface signal. The latter can be exploited for model validation using geologic observations such as the hiatus maps compiled by Vilacís *et al.* [88]. These maps offer a unique proxy for dynamic topography in time, obtained by a systematic global mapping of unconformities in the stratigraphic record (i.e. time gaps in continental sedimentary layers). A geodynamic flow model can produce synthetic predictions of hiatus regions (derived from dynamic topography fields) that can be compared to the real maps (Brown *et al.* [92]). If the flow is derived from an adjoint reconstruction, this means that there exists a relation between model validation and the way tomography is implemented in the cost function.

Better intuition for this link between tomography and dynamic topography can be developed by visualizing the various modelling components next to each other (figure 8): the true mantle structure, here represented by our MCM (figure 8a), the filtered version one would be able to actually infer seismically (figure 8b), the corresponding resolution lengths (figure 8d,e) and the so-called dynamic topography kernel that indicates the sensitivity of dynamic topography to density variations at depth (figure 8c, reproduced from Vilacís *et al.* [88] based on the reference viscosity profile of our MCM). With respect to this kernel function, the dynamic topography signal at the surface can be calculated by radially integrating a given mantle density structure. Note that the strongest sensitivity is in the upper mantle and decreases quite strongly below. The contribution to the total topographic signal depends additionally on the model wavelength (in the sense of spherical harmonics degrees given on the x-axis) as well as on the depth of a density anomaly.

Although in many observational studies density is derived from tomography, it is also an independent prediction and natural product of forward geodynamic models. This means that inference on dynamic topography can be approached with either technique. But as we have seen throughout our synthetic tomographic experiment, the true and tomographically filtered MCM structure can differ substantially throughout the mantle. In our case poor vertical resolution in the upper mantle (figure 8d) produces extensive anomalies. From a dynamical perspective, these are inconsistent with the convective system at high Rayleigh number ($Ra \approx 10^8$). This inconsistency can best be observed in the southern Atlantic, comparing figure 8a,b, where hot material from the Atlantic ridge is vertically smeared down to approximately 600 km depth through the seismic imaging. In the mid-mantle, again the narrower SOLA averaging kernels and lower overall mantle heterogeneity lead to a better recovery of structures. Hence, as a result of local resolution and the specific sensitivity in the dynamic topography kernel, different regions provide distinct levels of error that are accumulated in the final topographic field.

Given the general limitations of the tomographic approach, the question is whether a geodynamic model validation with an inaccurately reconstructed dynamic topography signal can still be used to better constrain the input parameters. As a thought experiment, imagine a seismic anomaly of relevant size in the mid- to upper mantle. The two tomographic error components that play a role are the extent of the imaged anomaly and its amplitude modified after filtering. The latter, as also seen in the RMS curves in figure 7, seems to be controlled more strongly by vertical resolution, while the horizontal resolution rather determines anomaly locations and wavelengths. But there is a trade-off implied by the topographic kernel between the vertical extent and the strength of an anomaly. The contribution of a vertically blurred structure with damped amplitude may, thus, be equal to that of a strong, but spatially more confined heterogeneity. Obviously, this is a highly simplified description of how the dynamic topography signal is composed. Nonetheless, while there might be some difficulty in obtaining the correct amplitudes

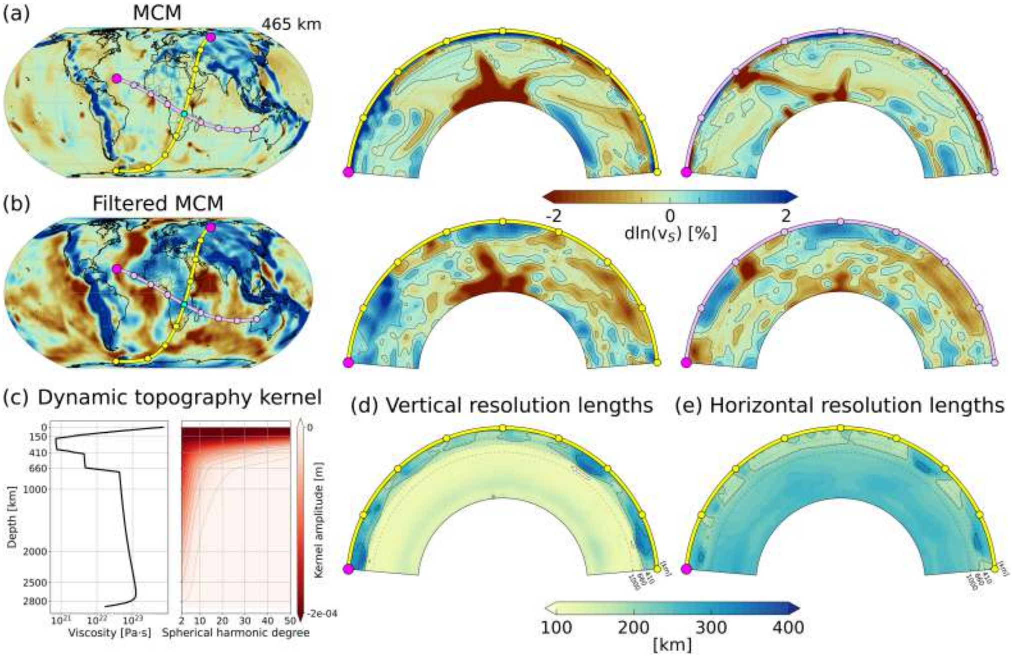

Figure 8. Side-by-side illustration of the components that control the dynamic topography signal at Earth's surface predicted from a tomographic image of mantle heterogeneity. (a; top row) Depth slice of the original MCM at 465 km and two cross-sections centred in southern Africa. Contour lines are drawn at 0 and ±0.5% S-wave velocity perturbation. (b; second row) Same as in (a) but for the tomographically filtered MCM, using averaging kernels with target lengths of 200/100 km, globally (same inversion set-up as in figure 6). (c) Reference viscosity profile of the original MCM and the associated dynamic (surface) topography kernel (following Figure 1 from Vilacís *et al.* [88]). (d,e) Cross-sections showing the vertical and horizontal resolution lengths associated with the tomographic filtering applied in (b). The available information on resolution effectively describes how the mantle structure is seen and modified by tomography. Dynamic topography predictions for the original and filtered structures are, thus, expected to differ, depending on local resolution and the associated changes in model amplitude and wavelengths.

and length scales of the underlying mantle heterogeneity, from these considerations, it seems feasible to obtain effective heterogeneity representations that can sufficiently explain the present-day dynamic topography. In our tomographic framework, this suggests testing the prediction of dynamic topography fields against different possible realizations of SOLA averaging kernels. We hypothesize that finding optimal horizontal resolution lengths should thereby be prioritized over vertical lengths first owing to the aforementioned size-density trade-off in the kernel (figure 8c).

Providing an effective density representation for the present-day state may, however, not suffice for accurately predicting the temporal evolution of dynamic topography with adjoint flow reconstructions. Any incorrectly depicted anomaly from the tomographic input model at present-day leads to a growing mismatch in the global flow history over time. Consequently, the wavelengths, locations and timing of dynamic uplift and subsidence will be systematically affected [93]. In addition to more realistic rheologies and lateral variations in viscosity, the influence of resolution lengths could offer another, yet unexplored explanation for spatio-temporal discrepancies between adjoint model results and observational constraints. A practical example of this is the continental-scale uplift history of Africa predicted in recent global flow reconstructions [33]. We note again that one of the main goals of retrodictions is to provide a framework for validating the underlying input parameters. If dynamic topography comparisons determine the success or failure of a geodynamic model, one should allow for a partial decoupling of the flow predictions from the tomographic forcing in the adjoint cost function. This has to be

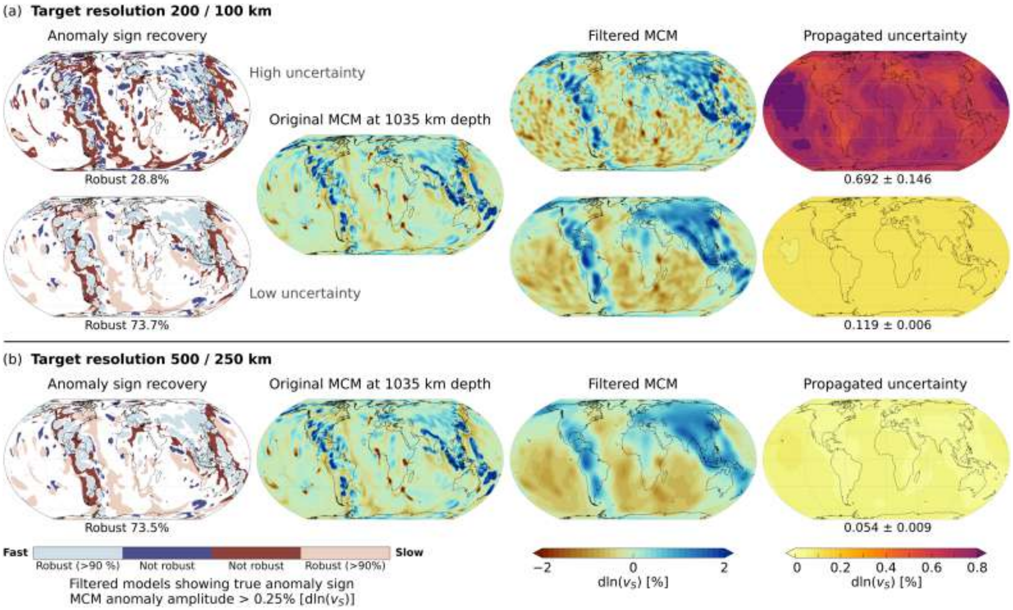

Figure 9. Illustration of 'robust' anomalies at 1035 km depth (first column), determined by comparing imaged seismic heterogeneity (third column) and model uncertainties (fourth column) with the original MCM (second column). The classification as robust means that more than 90% of tomographically filtered model values at a certain location correctly recover the sign of the true MCM anomaly after accounting for the SOLA model uncertainties. True anomalies are defined at a threshold of 0.25% S-wave velocity perturbation from the original MCM. White regions in the maps in the first column are below this threshold. Also, the filtered MCM and associated propagated uncertainties (mean of all uncertainties ± standard deviation below each map) are shown. (a) Maps for SOLA inversions with 200/100 km horizontal/vertical target-resolution kernels and two different trade-off parameters. In the upper row, the corresponding averaging kernels are forced to better fit the target, which leads to increased resolution at the cost of higher model uncertainty (in contrast to the middle row, using the same target kernels, but with less emphasis given to target fitting and lower uncertainties). (b) Maps for SOLA inversions with 500/250 km horizontal/vertical target-resolution lengths. The percentages of robust anomalies for a 200/100 km target and low uncertainty, and the 500/250 km target, are similar owing to the specific choices of trade-off parameters (note that some are different to those from figure 6). A list of trade-off parameters that have been used in each subfigure can be found in the electronic supplementary material.

explored in more detail in synthetic test cases, where both tomography and cost function are calibrated together. We further explain our ideas to accomplish this with SOLA in §3e.

(d) Model uncertainty and ensemble approaches

Up to this point, we have not touched on the consequences of stochastic uncertainty in the tomographic images. Incorporating propagated errors in the estimated SOLA averages is expected to change mostly the shape and location of anomalies [79] and only to some degree the RMS amplitudes that are rather controlled by target resolution (see figure 7). With our synthetic experiment, it is also possible to visualize the global effects of these tomographic model errors relative to the true MCM structure and to obtain a preliminary assessment of their dynamic impact (see figures 9 and 10). To define which anomalies in the original MCM are considered relevant, we use a threshold of 0.25% velocity perturbation. We then determine where more than 90% of the filtered model averages, within the range of inferred SOLA uncertainties, agree with the sign of an anomaly in the original MCM. These are here referred to as 'robustly' imaged anomalies. From a geodynamic perspective, we, thus, highlight where tomography would probably be able to reproduce the correct radial flow direction of the imaged buoyancy.

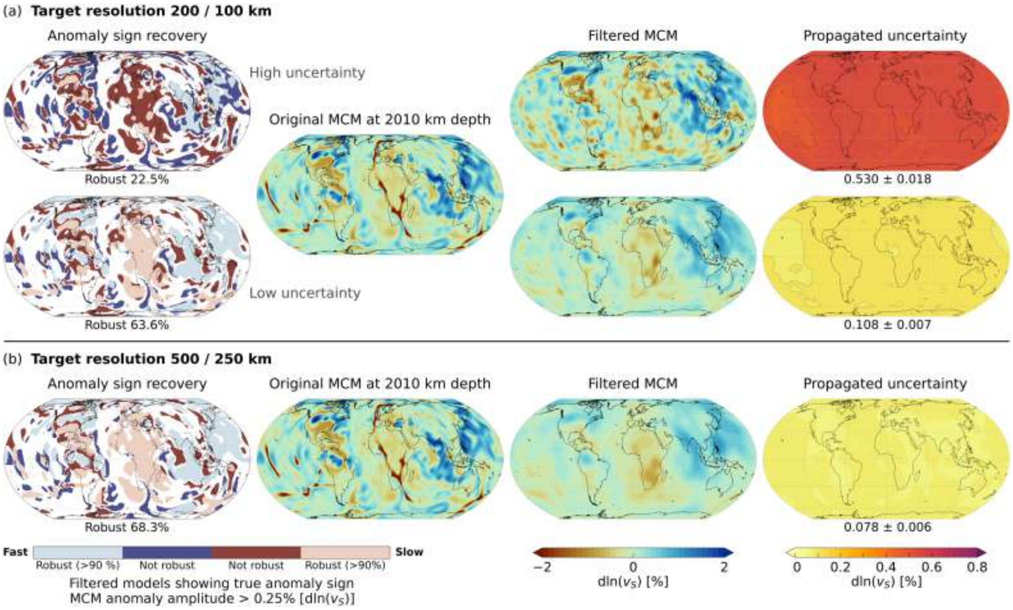

Figure 10. Illustration of robust anomalies at 2010 km depth. See figure 9 for details.

Interestingly, although the target resolution controls the wavelength of the filtered models, the sign of anomalies can be robustly recovered in many regions by both low and high-resolution SOLA inversions. We also observe that slow structures are more prone to being mistakenly flipped in sign compared to downgoing slabs owing to their weaker and spatially more focused temperature signature. Whether this happens for a specific plume depends on the amount of uncertainty propagating into the filtered model in that region (compare the second column with the third and fourth columns in figures 9 and 10). This provides guidance on where the local trade-off between the SOLA resolution-uncertainty properties could be further tuned if desired. For the target kernels with 200/100 km extent in figures 9a and 10a, we use two different trade-off parameters to demonstrate that changes in sign after filtering become more prevalent as uncertainties are increasing, for instance observed on a continental scale below Africa at 2010 km depth. Even so, the inversions can produce similar amounts of robust anomaly locations if the trade-off parameter is chosen to aim for low uncertainties at both 200/100 km (bottom row, figures 9a and 10a) and 500/250 km target kernels (figures 9b and 10b). In a few regions, again, anomalies are classified consistently as not robust, especially where two relevant true anomalies are close to each other, but one is considerably stronger and dominates the averaging process (for example, for most of the slow structures beneath South America at 2010 km depth).

In the low uncertainty cases, we obtain values of 63.6–73.7% of robustly recovered anomalies for the two target-resolution sizes. The present-day large-scale patterns of buoyancy can, thus, be captured well by both high- and low-resolution tomographic images, even if we account for propagated errors. This view on the dynamic effects of imaged mantle structure is, however, obviously simplified. The complete time-dependent flow behaviour is not exclusively controlled by the sign of an anomaly, but depends on its volumetric extent. Dynamic effects of implementing one or the other tomographic realization in flow reconstructions can, thus, not be inferred solely from the considerations above. This highlights that even if we can give specific uncertainty values to tomographic models (or in Bayesian frameworks full probability densities), it is often not known how to make practical use of this information. In case of the computationally challenging flow-reconstruction problem, there is moreover a lack of techniques for propagating errors from tomography through the geodynamic adjoint equations in time.

To cope with this issue, an established approach in other disciplines in numerical weather prediction (e.g. [94]), is to work with model ensembles. Different model realizations are expected to produce alternative flow histories that can subsequently be validated using various observations, with a focus on dynamic topography. Although this is indeed a useful direction for geodynamic modelling in future, two major difficulties need to be considered. On one hand, retrodiction models generally require immense computational resources since several iterations of expensive forward MCM and adjoint model runs are performed. This obviously limits the number of ensemble members one can effectively incorporate in the analysis. On the other hand, as we have seen through our filtering exercise, a given tomography can usually not reveal Earth structure at all scales and locations equally well. Both issues together have the following consequences: (1) geodynamicists need to be highly selective about which tomographic image realizations should be considered and (2) the ideas on representing resolution length scales in the adjoint cost function from §3c need to be incorporated first to make the most of each single ensemble member simulation.

(e) Retrodiction workflow with SOLA

Finally, we outline in what way SOLA results could potentially be incorporated in the workflow of geodynamic mantle flow retrodictions. Considering the concurrent tasks of accounting for geodynamic-tomographic length-scale discrepancies and stochastic model errors, we propose to approach this question in two different steps.

(i) We first need to better understand the influence of resolution in the cost function equation (3.1) of the geodynamic adjoint models. This implies that one should seek a physically motivated misfit term that can reflect the tomographic resolution bias in a given image. The local SOLA averages provide us explicitly with averaging or resolution lengths for this purpose. Within the associated volume, the geodynamic model can develop smaller-scale structure if required by the dynamic flow system, as long as the volumetric average stays close to the tomographic reference. Thus, the present-day buoyancy would be partially decoupled from tomography while still fitting the actual image. It is, therefore, an important feature of SOLA that both the tomographic operators and the corresponding image can be provided together. The exact way of implementing them together in the adjoint method to best exploit the resolution information will be the subject of future studies. One possibility would be to test different strategies in synthetic closed-loop experiments, whereby a reference MCM is used to define the true state like in the present study. A range of 'standard' adjoint models (i.e. using the cost function in equation (3.1)) could be created with different SOLA images of the reference MCM, including low- and high-resolution scenarios controlled through the choice of target kernel size and trade-off parameter (see §2d). Also, mixed scenarios should be considered, encountered when local higher-resolution images are superimposed on a global long wavelength model. In a second set of adjoint models, the different standard runs could be enhanced by new cost functions that include regularization terms that inform the model about the local SOLA averaging lengths of the corresponding images. To assess the success of each approach, one can exploit the fact that the reference MCM produces a specific history of dynamic topography. The true surface evolution may not be matched well by an adjoint flow reconstruction if tomography is poorly implemented (see §3c). Comparing the dynamic topography predictions from such a set of self-consistent geodynamic adjoint models would, therefore, offer an empirical approach to determine useful adjustments in the cost function.

(ii) Only as a second step, the stochastic tomographic model uncertainties can effectively be addressed using an ensemble approach, whereby a number of flow reconstructions are performed for several realizations of the tomographic constraint. Alternative realizations of a given SOLA image can be obtained by drawing samples from the distribution of

> data errors and incorporating them in the SOLA averages via filtering with the GIP approach, as demonstrated in [79]. As a result, mantle anomalies appear at varying locations and with distinct amplitudes and shapes in different tomographic models, each giving rise to different dynamic flow back in geologic time in the adjoint reconstructions. In the pursuance of obtaining tighter constraints on the mantle evolution from a very limited number of possible adjoint model runs, one should consequently aim for a strong variability in such a flow model ensemble. Guidance on the selection of a certain set of tomographic input models can be obtained by comparison of the vertical and horizontal resolution lengths with dynamic topography kernels (figure 8) and by the analysis of robust buoyancy recovery (figures 9 and 10). The ensemble can again incorporate both high- and low-resolution images corresponding to more data-driven versus more model-driven flow reconstructions, respectively. In the case of more data-driven retrodictions, with high-resolution images, one should keep in mind that a larger number of ensemble members is necessary to capture the spread of possible flow trajectories. Another intriguing option are ensemble members based on mixed-resolution scenarios. They would allow for testing how large-scale tomographic model errors affect the reconstructed flow behaviour in a certain target region where higher-resolution imaging might be available. An important fact to also keep in mind is that SOLA offers the possibility to include error components that can deviate from the assumption of normally distributed errors such that models with systematic bias can be created [79].

With the above described steps (i) and (ii), we, thus, propose the following workflow for real retrodiction applications: first, a reference geodynamic forward simulation (an MCM) is run with a set of input parameters for describing the plate motion history, rheology and energy budget (essentially CMB temperature and internal heating). Going into the adjoint method, we then perform synthetic flow reconstructions first, where tomographically filtered images from seismic data predicted for the MCM are employed. Making use of the ideas developed in (i) and (ii), one can then determine a useful cost function for the geodynamic-tomographic configuration and a set of SOLA tomographic realizations that should lead to a relevant ensemble of flow retrodictions. The good statistical fit of seismic observations and predictions made from current MCMs (e.g. for filtered mantle heterogeneity [38] and traveltimes [16]) ensures that this synthetically derived tomographic set-up can also be applied to real data in the actual retrodiction experiment. To account for the geodynamic–tomographic length-scale discrepancy in the cost function, tomographic filtering with the GIP approach [79] has to be performed with each adjoint iteration. This necessitates efficient calculations of synthetic seismic data for each individually evolving forward MCM in the ensemble. Using the GIP approach is thereby essential to avoid additional errors from the unphysical reparametrization that would be encountered in the classical filtering approach via the resolution operator. Finally, the ensemble of flow histories should be validated through the comparison of predicted dynamic topography in time with geologic information, as provided by global maps of hiatus surfaces [88]. More robust conclusions could then be drawn from the analysis of these resolution-informed retrodictions.

The set-up that we presented here provides the foundation for realizing this workflow. Future developments in the SOLA global tomographic framework include the uptake of surface wave information [95] and normal mode data [65]. These can complement body-wave traveltimes and, thus, further improve resolution (especially in the upper mantle) in line with comparable global tomographies (e.g. [96–99]). We also emphasize again that the proposed workflow focuses specifically on the integration of tomographic errors for investigating their geodynamic consequences. A mathematically more general uncertainty analysis would require different techniques (e.g. making use of Hessian information [100,101]) that still need to be developed and made applicable to mantle flow reconstructions. Note that this would also require a quantification of absolute errors in local seismic velocities that are more difficult to quantify than the uncertainties in SOLA model averages we provide here. These SOLA uncertainties, however, are well-defined and allow the construction of small selective ensembles required in face of the computational burden of adjoint flow models. Synthetic closed-loop retrodiction experiments with full control on the tomographic input, as provided by SOLA, thus, pave the way for testing such integration strategies in a fully consistent manner and instruct future retrodiction experiments on how the different aspects of tomographic uncertainty can be taken into account.

4. Conclusion

Synthetic deep Earth studies are becoming increasingly important to advance our knowledge on the mantle's properties and its evolution in the recent geologic past. In particular, they enable a quantitative understanding of all relevant observations in the context of an integrative geodynamic framework, as provided by adjoint reconstructions of past mantle flow. Turning to these time-dependent models makes it possible to connect observations that are commonly dealt with in different disciplines, to overcome existing data and model uncertainties. By making use of the SOLA Backus–Gilbert method, we developed a workflow on how tomographic uncertainty could possibly be dealt with in this regard. Tomographic images are commonly incorporated as direct observations of the present-day state of the mantle, contradicting the fact that they are the result of inverse modelling. As we have demonstrated with our synthetic experiment, the time-dependent geodynamic modelling, thus, requires an appropriate account of local length scale and amplitude discrepancies with respect to tomography. Using the SOLA method thereby has the advantage that one has full information on resolution and model uncertainties available, which allows for quick testing of different tomographic realizations. This opens up a new empirical direction for inferring mantle dynamics based on data assimilation with uncertain seismological observations.

Most importantly, the final state of geodynamic adjoint models should not be forced to immediately match the tomographically estimated reference state owing to the spatially variable resolution and quality of tomographic images. Instead, only after tomographic filtering is a one-to-one comparison physically meaningful throughout the model domain, which is especially important for robust inferences in oceanic regions and in the proximity to major phase transitions. Formally implementing this in the geodynamic adjoints, through a practical misfit function and going towards ensemble simulations, allows us to obtain more accurate predictions of dynamic topography back in time, which should be driven by the convection process rather than the input of an uncertain tomographic reference. This ultimately makes it possible to obtain tighter constraints on geodynamic parameter choices through the validation of flow trajectories against geological observations.

Data accessibility. The synthetic dataset used for the tomographic inversions is provided in electronic supplementary material [102].

Declaration of AI use. We have not used AI-assisted technologies in creating this article.

Authors' contributions. R.F.: conceptualization, data curation, formal analysis, funding acquisition, investigation, methodology, software, validation, visualization, writing—original draft, writing—review and editing; B.S.A.S.: conceptualization, funding acquisition, investigation, project administration, software, supervision, validation, writing—review and editing; I.L.S.: investigation, software, validation, visualization, writing—review and editing; C.Z.: investigation, software, supervision, validation, writing—review and editing.

All authors gave final approval for publication and agreed to be held accountable for the work performed therein.

Conflict of interest declaration. We declare we have no competing interests.

Funding. R.F. and B.S.A.S. acknowledge support from the Deutsche Forschungsgemeinschaft (DFG) through the research grant no. SCHU 2914/7-1 project no. 456788150 and the UPLIFT Research Training Group, project no. 440512084; I.L.S through the DeepDyn priority programme, project no. 521319093. Computing resources were provided by the Institute of Geophysics of LMU Munich (Oeser *et al.* [103]) funded by the DFG project nos. 495931446 and 518204048. The authors gratefully acknowledge the Gauss Centre for Supercomputing e.V. (www.gauss-centre.eu) for funding this project by providing computing time on the GCS Supercomputer SuperMUC at Leibniz Supercomputing Centre (www.lrz.de).

Acknowledgements. We thank editor Sergei Lebedev, Siavash Ghelichkhan and an anonymous reviewer for their constructive feedback. We are grateful to Hans-Peter Bunge and Isabel Papanagnou for fruitful discussions and thank Berta Vilacís for providing a code for reproducing fig. 1 of Vilacís *et al.* [88] with the viscosity profile of our MCM. We made use of the publicly available scientific colour maps from Crameri *et al.* [104]. Seismic station data were downloaded and processed using ObsPy [105].

References

1. Cathles L, Fjeldskar W, Lenardic A, Romanowicz B, Seales J, Richards M. 2023 Influence of the asthenosphere on earth dynamics and evolution. *Sci. Rep.* **13**, 13367. (doi:10.1038/s41598-023-39973-y)
2. Hayek JN, Stotz IL, Bunge HP, Carena S. 2025 First-order global stress patterns inferred from upper mantle flow models. *Proc. R. Soc. A* **481**, 20240969. (doi:10.1098/rspa.2024.0969)
3. Austermann J, Mitrovica JX, Huybers P, Rovere A. 2017 Detection of a dynamic topography signal in last interglacial sea-level records. *Sci. Adv.* **3**, e1700457. (doi:10.1126/sciadv.1700457)
4. Dannberg J, Gassmöller R, Thallner D, LaCombe F, Sprain C. 2024 Changes in core–mantle boundary heat flux patterns throughout the supercontinent cycle. *Geophys. J. Int.* **237**, 1251–1274. (doi:10.1093/gji/ggae075)
5. Bunge HP, Richards M. 1996 The origin of large-scale structure in mantle convection: effects of plate motions and viscosity stratification. *Geophys. Res. Lett.* **23**, 2987–2990. (doi:10.1029/96GL02522)
6. Zhong S, Zhang N, Li ZX, Roberts JH. 2007 Supercontinent cycles, true polar wander, and very long-wavelength mantle convection. *Earth Planet. Sci. Lett.* **261**, 551–564. (doi:10.1016/j.epsl.2007.07.049)
7. Davies D, Davies J. 2009 Thermally-driven mantle plumes reconcile multiple hot-spot observations. *Earth Planet. Sci. Lett.* **278**, 50–54. (doi:10.1016/j.epsl.2008.11.027)
8. Stadler G, Gurnis M, Burstedde C, Wilcox LC, Alisic L, Ghattas O. 2010 The dynamics of plate tectonics and mantle flow: from local to global scales. *Science* **329**, 1033–1038. (doi:10.1126/science.1191223)
9. Davies DR, Davies JH, Bollada PC, Hassan O, Morgan K, Nithiarasu P. 2013 A hierarchical mesh refinement technique for global 3-D spherical mantle convection modelling. *Geosci. Model Dev.* **6**, 1095–1107. (doi:10.5194/gmd-6-1095-2013)
10. Schuberth BSA, Bunge HP, Steinle-Neumann G, Moder C, Oeser J. 2009 Thermal versus elastic heterogeneity in high-resolution mantle circulation models with pyrolite composition: high plume excess temperatures in the lowermost mantle. *Geochem. Geophys. Geosyst.* **10**, Q01W01. (doi:10.1029/2008GC002235)
11. Stotz IL, Iaffaldano G, Davies DR. 2018 Pressure-driven Poiseuille flow: a major component of the torque-balance governing Pacific plate motion. *Geophys. Res. Lett.* **45**, 117–125. (doi:10.1002/2017GL075697)
12. Seton M *et al.* 2012 Global continental and ocean basin reconstructions since 200 Ma. *Earth Sci. Rev.* **113**, 212–270. (doi:10.1016/j.earscirev.2012.03.002)
13. Müller RD *et al.* 2016 Ocean basin evolution and global-scale plate reorganization events since Pangea breakup. *Ann. Rev. Earth Planet. Sci.* **44**, 107–138. (doi:10.1146/annurev-earth-060115-012211)
14. Müller RD, Flament N, Cannon J, Tetley MG, Williams SE, Cao X, Bodur OF, Zahirovic S, Merdith A. 2022 A tectonic-rules-based mantle reference frame since 1 billion years ago—implications for supercontinent cycles and plate–mantle system evolution. *Solid Earth* **13**, 1127–1159. (doi:10.5194/se-13-1127-2022)
15. Chen YW, Wu J, Bunge HP, Stotz I, Robl G, Schuberth BSA. 2025 Tomopac2: an unfolded-slab plate reconstruction validated via mantle circulation models in a closed-loop experiment. *Proc. R. Soc. A* **481**, 20240726. (doi:10.1098/rspa.2024.0726)
16. Schuberth BSA, Zaroli C, Nolet G. 2012 Synthetic seismograms for a synthetic Earth: long-period P- and S-wave traveltime variations can be explained by temperature alone. *Geophys. J. Int.* **188**, 1393–1412. (doi:10.1111/j.1365-246X.2011.05333.x)
17. Schuberth BSA, Zaroli C, Nolet G. 2015 Traveltime dispersion in an isotropic elastic mantle: strong lower-mantle signal in differential-frequency residuals. *Geophys. J. Int.* **203**, 2099–2118. (doi:10.1093/gji/ggv389)

18. Davies DR, Goes S, Lau HCP. 2015 Thermally dominated deep mantle LLSVPs: a review. In *The Earth's heterogeneous mantle* (eds A Khan, F Deschamps), pp. 441–477. Springer, Cham: Springer Geophysics. (doi:10.1007/978-3-319-15627-9_14)
19. Becker TW, Kellogg JB, Ekström G, O'Connell RJ. 2003 Comparison of azimuthal seismic anisotropy from surface waves and finite strain from global mantle-circulation models. *Geophys. J. Int.* **155**, 696–714. (doi:10.1046/j.1365-246X.2003.02085.x)
20. Becker TW, Chevrot S, Schulte-Pelkum V, Blackman DK. 2006 Statistical properties of seismic anisotropy predicted by upper mantle geodynamic models. *J. Geophys. Res.: Solid Earth* **111**, B08309. (doi:10.1029/2005JB004095)
21. Stotz IL. 2025 Predictions of asthenosphere flow from Couette/Poiseuille models compared to seismic anisotropy and mantle circulation models. *Proc. R. Soc. A* **481**, 20250085. (doi:10.1098/rspa.2025.0085)
22. Colli L, Ghelichkhan S, Bunge HP. 2016 On the ratio of dynamic topography and gravity anomalies in a dynamic Earth. *Geophys. Res. Lett.* **43**, 2510–2516. (doi:10.1002/2016GL067929)
23. Davies DR, Ghelichkhan S, Hoggard M, Valentine A, Richards F. 2023 Chapter 11—Observations and models of dynamic topography: current status and future directions. In *Dynamics of plate tectonics and mantle convection* (ed. JC Duarte), pp. 223–269. Elsevier. (doi:10.1016/B978-0-323-85733-8.00017-2)
24. Davies JH *et al.* 2025 How to assess similarities and differences between mantle circulation models and Earth using disparate independent observations. *Proc. R. Soc. A* **481**, 20240827. (doi:10.1098/rspa.2024.0827)
25. Bunge HP, Hagelberg CR, Travis BJ. 2003 Mantle circulation models with variational data-assimilation: inferring past mantle flow and structure from plate motion histories and seismic tomography. *Geophys. J. Int.* **2**, 280–301. (doi:10.1046/j.1365-246X.2003.01823.x)
26. Ismail-Zadeh A, Schubert G, Tsepelev I, Korotkii A. 2004 Inverse problem of thermal convection: numerical approach and application to mantle plume restoration. *Phys. Earth Planet. Inter.* **145**, 99–114. (doi:10.1016/j.pepi.2004.03.006)
27. Liu LJ, Gurnis M. 2008 Simultaneous inversion of mantle properties and initial conditions using an adjoint of mantle convection. *J. Geophys. Res.* **113**, B08405. (doi:10.1029/2008JB005594)
28. Spasojevic S, Liu L, Gurnis M. 2009 Adjoint models of mantle convection with seismic, plate motion, and stratigraphic constraints: North America since the Late Cretaceous. *Geochem. Geophys. Geosyst.* **10**. (doi:10.1029/2008GC002345)
29. Shephard GE, Müller RD, Liu L, Gurnis M. 2010 Miocene drainage reversal of the Amazon River driven by plate-mantle interaction. *Nat. Geosci.* **3**, 870–875. (doi:10.1038/ngeo1017)
30. Horbach A, Bunge HP, Oeser J. 2014 The adjoint method in geodynamics: derivation from a general operator formulation and application to the initial condition problem in a high resolution mantle circulation model. *GEM—Int. J. Geomath.* **5**, 163–194. (doi:10.1007/s13137-014-0061-5)
31. Colli L, Ghelichkhan S, Bunge HP, Oeser J. 2018 Retrodictions of Mid Paleogene mantle flow and dynamic topography in the Atlantic region from compressible high resolution adjoint mantle convection models: sensitivity to deep mantle viscosity and tomographic input model. *Gondwana Res.* **53**, 252–272. (doi:10.1016/j.gr.2017.04.027). Rifting to Passive Margins.
32. Price MG, Davies JH. 2018 Profiling the robustness, efficiency and limits of the forward-adjoint method for 3-D mantle convection modelling. *Geophys. J. Int.* **212**, 1450–1462. (doi:10.1093/gji/ggx489)
33. Ghelichkhan S, Bunge HP, Oeser J. 2021 Global mantle flow retrodictions for the early Cenozoic using an adjoint method: evolving dynamic topographies, deep mantle structures, flow trajectories and sublithospheric stresses. *Geophys. J. Int.* **226**, 1432–1460. (doi:10.1093/gji/ggab108)
34. Bunge HP, Horbach A, Colli L, Ghelichkhan S, Vilacís B, Hayek JN. 2023 In *Geodynamic data assimilation: techniques and observables to construct and constrain time-dependent earth models*. Special Publications of the International Union of Geodesy and Geophysics, pp. 311–325. UK: Cambridge University Press.
35. Bello L, Coltice N, Rolf T, Tackley PJ. 2014 On the predictability limit of convection models of the Earth's mantle. *Geochem. Geophys. Geosyst.* **15**, 2319–2328. (doi:10.1002/2014GC005254)

36. Colli L, Bunge HP, Schuberth BSA. 2015 On retrodictions of global mantle flow with assimilated surface velocities. *Geophys. Res. Lett.* **42**, 8341–8348. (doi:10.1002/2015gl066001)
37. Colli L, Bunge HP, Oeser J. 2020 Impact of model inconsistencies on reconstructions of past mantle flow obtained using the adjoint method. *Geophys. J. Int.* **221**, 617–639. (doi:10.1093/gji/ggaa023)
38. Schuberth BSA, Bunge HP, Ritsema J. 2009 Tomographic filtering of high-resolution mantle circulation models: can seismic heterogeneity be explained by temperature alone? *Geochem. Geophys. Geosyst.* **10**, Q05W03. (doi:10.1029/2009GC002401)
39. Zaroli C. 2016 Global seismic tomography using Backus–Gilbert inversion. *Geophys. J. Int.* **207**, 876–888. (doi:10.1093/gji/ggw315)
40. Pijpers F, Thompson M. 1992 Faster formulations of the optimally localized averages method for helioseismic inversions. *Astron. Astrophys.* **262**, L33–L36.
41. Zaroli C. 2019 Seismic tomography using parameter-free Backus–Gilbert Inversion. *Geophys. J. Int.* **218**, 619–630. (doi:10.1093/gji/ggz175)
42. Nolet G. 2008 *A breviary of seismic tomography*. New York: Cambridge University Press.
43. Nerlich R, Colli L, Ghelichkhan S, Schuberth B, Bunge HP. 2016 Constraining central Neo-Tethys Ocean reconstructions with mantle convection models. *Geophys. Res. Lett.* **43**, 9595–9603. (doi:10.1002/2016gl070524)
44. Stotz IL, Iaffaldano G, Davies DR. 2017 Late Miocene Pacific plate kinematic change explained with coupled global models of mantle and lithosphere dynamics. *Geophys. Res. Lett.* **44**, 7177–7186. (doi:10.1002/2017GL073920)
45. Lin YA, Colli L, Wu J, Schuberth BSA. 2020 Where are the proto-South China Sea slabs? SE Asian plate tectonics and mantle flow history from global mantle convection modeling. *J. Geophys. Res.: Solid Earth* **125**, e2020JB019758. (doi:10.1029/2020JB019758)
46. Calvelage CM, Wu J, Colli L, Lin YA, Zheng Y. 2024 Linking deep-time subduction history to modern day expressions of dynamic topography. *Proc. R. Soc. A* **480**, 20240254. (doi:10.1098/rspa.2024.0254)
47. Baumgardner JR. 1985 Three-dimensional treatment of convective flow in the Earth's mantle. *J. Stat. Phys.* **39**, 501–511. (doi:10.1007/BF01008348)
48. Bunge HP, Baumgardner J. 1995 Mantle convection modeling on parallel virtual machines. *Comput. Phys.* **9**, 207–215. (doi:10.1063/1.168525)
49. Becker TW, Boschi L. 2002 A comparison of tomographic and geodynamic mantle models. *Geochem. Geophys. Geosyst.* **3**, 1003. (doi:10.1029/2001GC000168)
50. Koelemeijer P, Schuberth B, Davies D, Deuss A, Ritsema J. 2018 Constraints on the presence of post-perovskite in Earth's lowermost mantle from tomographic-geodynamic model comparisons. *Earth Planet. Sci. Lett.* **494**, 226–238. (doi:10.1016/j.epsl.2018.04.056)
51. Chust TC, Steinle-Neumann G, Dolejš D, Schuberth BSA, Bunge HP. 2017 MMA-EoS: a computational framework for mineralogical thermodynamics. *J. Geophys. Res.* **122**, 9881–9920. (doi:10.1002/2017JB014501)
52. Stixrude L, Lithgow-Bertelloni C. 2007 Influence of phase transformations on lateral heterogeneity and dynamics in Earth's mantle. *Earth Planet. Sci. Lett.* **263**, 45–55. (doi:10.1016/j.epsl.2007.08.027)
53. Schuberth BS, Bigalke T. 2021 From mantle convection to seismic observations: quantifying the uncertainties related to anelasticity. American Geophysical Union (AGU) Geophysical Monograph Series. In *Mantle convection and surface expressions*, pp. 97–119.
54. Komatitsch D *et al.* 2023 SPECFEM/specfem3d_globe: SPECFEM3D_GLOBE v8.1.0. (doi:10.5281/zenodo.10411115).
55. Ekström G, Nettles M, Dziewonski AM. 2012 The global CMT project 2004–2010: centroid-moment tensors for 13 017 earthquakes. *Phys. Earth Planet. Inter.* **200–201**, 1–9. (doi:10.1016/j.pepi.2012.04.002)
56. Dahlen FA, Hung SH, Nolet G. 2000 Fréchet kernels for finite-frequency traveltimes—I theory. *Geophys. J. Int.* **141**, 157–174. (doi:10.1046/j.1365-246x.2000.00070.x)
57. Zaroli C, Debayle E, Sambridge M. 2010 Frequency-dependent effects on global S-wave traveltimes: wavefront-healing, scattering and attenuation. *Geophys. J. Int.* **182**, 1025–1042. (doi:10.1111/j.1365-246X.2010.04667.x)
58. Chaves CAM, Ritsema J, Koelemeijer P. 2020 Comparing ray-theoretical and finite-frequency teleseismic traveltimes: implications for constraining the ratio of S-wave to P-wave velocity variations in the lower mantle. *Geophys. J. Int.* **224**, 1540–1552. (doi:10.1093/gji/ggaa534)

59. Backus GE, Gilbert JF. 1967 Numerical applications of a formalism for geophysical inverse problems. *Geophys. J. Int.* **13**, 247–276. (doi:10.1111/j.1365-246X.1967.tb02159.x)
60. Backus GE, Gilbert JF. 1968 The resolving power of gross Earth data. *Geophys. J. Int.* **16**, 169–205. (doi:10.1111/j.1365-246X.1968.tb00216.x)
61. Backus GE, Gilbert JF. 1970 Uniqueness in the inversion of inaccurate gross Earth data. *Phil. Trans. R. Soc. Lond. A* **266**, 123–192. (doi:10.1098/rsta.1970.0005)
62. Zaroli C, Koelemeijer P, Lambotte S. 2017 Toward seeing the Earth's interior through unbiased tomographic lenses. *Geophys. Res. Lett.* **44**, 11399–11408. (doi:10.1002/2017GL074996)
63. Al-Attar D. 2021 Linear inference problems with deterministic constraints. (http://arxiv.org/abs/2104.12256)
64. Latallerie F, Zaroli C, Lambotte S, Maggi A. 2022 Analysis of tomographic models using resolution and uncertainties: a surface wave example from the Pacific. *Geophys. J. Int.* **230**, 893–907. (doi:10.1093/gji/ggac095)
65. Restelli F, Zaroli C, Koelemeijer P. 2024 Robust estimates of the ratio between S- and P-wave velocity anomalies in the Earth's mantle using normal modes. *Phys. Earth Planet. Inter.* **347**, 107135. (doi:10.1016/j.pepi.2023.107135)
66. Mag AM, Zaroli C, Koelemeijer P. 2025 Bridging the gap between SOLA and deterministic linear inferences in the context of seismic tomography. *Geophys. J. Int.* **242**, ggaf131. (doi:10.1093/gji/ggaf131)
67. Pijpers F, Thompson M. 1994 The SOLA method for helioseismic inversion. *Astron. Astrophys.* **281**, 231–240.
68. Freissler R, Schuberth BSA, Zaroli C. 2024 A concept for the global assessment of tomographic resolution and uncertainty. *Geophys. J. Int.* **238**, 992–1012. (doi:10.1093/gji/ggae178)
69. Peterson M, Vollmer C, Brogan R, Stracuzzi DJ, Young CJ. 2020 Generating uncertainty distributions for seismic signal onset times. *Bull. Seismol. Soc. Am.* **111**, 11–20. (doi:10.1785/0120200125)
70. Marquering H, Dahlen FA, Nolet G. 1999 Three-dimensional sensitivity kernels for finite-frequency traveltimes: the banana-doughnut paradox. *Geophys. J. Int.* **137**, 805–815. (doi:10.1046/j.1365-246x.1999.00837.x)
71. Hung SH, Dahlen F, Nolet G. 2000 Fréchet kernels for finite-frequency traveltimes—II Examples. *Geophys. J. Int.* **141**, 175–203. (doi:10.1046/j.1365-246x.2000.00072.x)
72. To A, Romanowicz B. 2009 Finite frequency effects on global S diffracted traveltimes. *Geophys. J. Int.* **179**, 1645–1657. (doi:10.1111/j.1365-246x.2009.04359.x)
73. Mercerat E, Nolet G. 2012 Comparison of ray-based and adjoint-based sensitivity kernels for body-wave seismic tomography. *Geophys. Res. Lett.* **39**, L12301. (doi:10.1029/2012GL052002)
74. Zaroli C. 2010 Global multiple-frequency S-wave tomography of the Earth's mantle. PhD thesis, EOST/IPGS, Université de Strasbourg.
75. Megnin C, Romanowicz B. 1999 The effects of the theoretical formalism and data selection on mantle models derived from waveform tomography. *Geophys. J. Int.* **138**, 366–380. (doi:10.1046/j.1365-246X.1999.00869.x)
76. Ritsema J, McNamara AK, Bull AL. 2007 Tomographic filtering of geodynamic models: implications for model interpretation and large-scale mantle structure. *J. Geophys. Res.* **112**, B01303. (doi:10.1029/2006JB004566)
77. Bull A, McNamara A, Ritsema J. 2009 Synthetic tomography of plume clusters and thermochemical piles. *Earth Planet. Sci. Lett.* **278**, 152–162. (doi:10.1016/j.epsl.2008.11.018)
78. Simmons NA, Schuberth BSA, Myers SC, Knapp DR. 2019 Resolution and covariance of the LLNL-G3D-JPS global seismic tomography model: applications to travel time uncertainty and tomographic filtering of geodynamic models. *Geophys. J. Int.* **217**, 1543–1557. (doi:10.1093/gji/ggz102)
79. Freissler R, Zaroli C, Lambotte S, Schuberth BSA. 2020 Tomographic filtering via the generalized inverse: a way to account for seismic data uncertainty. *Geophys. J. Int.* **223**, 254–269. (doi:10.1093/gji/ggaa231)
80. Davaille A, Romanowicz B. 2020 Deflating the LLSVPs: bundles of mantle thermochemical plumes rather than thick stagnant 'Piles'. *Tectonics* **39**, e2020TC006265. (doi:10.1029/2020TC006265)

81. Ghelichkhan S, Bunge HP. 2018 The adjoint equations for thermochemical compressible mantle convection: derivation and verification by twin experiments. *Proc. R. Soc. A* **474**. (doi:10.1098/rspa.2018.0329)
82. Davies DR, Goes S, Davies J, Schuberth B, Bunge HP, Ritsema J. 2012 Reconciling dynamic and seismic models of Earth's lower mantle: the dominant role of thermal heterogeneity. *Earth Planet. Sci. Lett.* **353–354**, 253–269. (doi:10.1016/j.epsl.2012.08.016)
83. Robl G, Schuberth BSA, Papanagnou I, Thomas C. 2025 From seismic models to mantle temperatures: uncertainties related to mineralogical complexities and limited tomographic resolution. *Geophys. J. Int.* **241**, 2003–2027. (doi:10.1093/gji/ggaf141)
84. Ghelichkhan S, Gibson A, Davies DR, Kramer SC, Ham DA. 2024 Automatic adjoint-based inversion schemes for geodynamics: reconstructing the evolution of Earth's mantle in space and time. *Geosci. Model Dev.* **17**, 5057–5086. (doi:10.5194/gmd-17-5057-2024)
85. Li D, Gurnis M, Stadler G. 2017 Towards adjoint-based inversion of time-dependent mantle convection with nonlinear viscosity. *Geophys. J. Int.* **209**, 86–105. (doi:10.1093/gji/ggw493)
86. Papanagnou I, Schuberth BSA, Thomas C. 2022 Geodynamic predictions of seismic structure and discontinuity topography of the mantle transition zone. *Geophys. J. Int.* **234**, 355–378. (doi:10.1093/gji/ggac478)
87. Murakami M, Hirose K, Kawamura K, Sata N, Ohishi Y. 2004 Post-perovskite phase transition in $MgSiO_3$. *Science* **304**, 855–858. (doi:10.1126/science.1095932)
88. Vilacís B, Brown H, Bunge HP, Carena S, Hayek JN, Stotz IL, Wang ZR, Friedrich AM. 2024 Dynamic topography and the planform of mantle convection since the Jurassic inferred from global continental hiatus maps. *Proc. R. Soc. A* **480**, 20240311. (doi:10.1098/rspa.2024.0311)
89. Richards MA, Hager BH. 1984 Geoid anomalies in a dynamic Earth. *J. Geophys. Res.* **89**, 5987–6002. (doi:10.1029/JB089iB07p05987)
90. Hager B, Clayton R, Richards M, Comer R, Dziewonski A. 1985 Lower mantle heterogeneity, dynamic topography and the geoid. *Nature* **313**, 541–545. (doi:10.1038/313541a0)
91. Hager BH, Richards MA. 1989 Long-wavelength variations in Earths geoid—physical models and dynamical implications. *Phil. Trans. R. Soc. A* **328**, 309–327. (doi:10.1098/rsta.1989.0038)
92. Brown H, Vilacís B, Stotz IL, Bunge H-P 2026 Synthetic geological hiatus maps as a tool for assessing reconstructions of past dynamic topography. *Proc. R. Soc. A* **482**, 20250249. (doi:10.1098/rspa.2025.0249)
93. Taiwo A, Bunge HP, Schuberth BSA, Colli L, Vilacis B. 2023 Robust global mantle flow trajectories and their validation via dynamic topography histories. *Geophys. J. Int.* **234**, 2160–2179. (doi:10.1093/gji/ggad188)
94. Schwartz CS, Romine GS, Sobash RA, Fossell KR, Weisman ML. 2019 NCAR's real-time convection-allowing ensemble project. *Bull. Am. Meteorol. Soc.* **100**, 321–343. (doi:10.1175/BAMS-D-17-0297.1)
95. Latallerie F, Zaroli C, Lambotte S, Maggi A, Walker A, Koelemeijer P. 2025 Towards surface wave tomography with 3D resolution and uncertainty. *Seismica* **4**. (doi:10.26443/seismica.v4i2.1407)
96. Ritsema J, Deuss A, van Heijst HJ, Woodhouse JH. 2011 S40RTS: a degree-40 shear-velocity model for the mantle from new Rayleigh wave dispersion, teleseismic traveltime and normal-mode splitting function measurements. *Geophys. J. Int.* **184**, 1223–1236. (doi:10.1111/j.1365-246X.2010.04884.x)
97. Auer L, Boschi L, Becker TW, Nissen-Meyer T, Giardini D. 2014 Savani: a variable resolution whole-mantle model of anisotropic shear velocity variations based on multiple data sets. *J. Geophys. Res.: Solid Earth* **119**, 3006–3034. (doi:10.1002/2013JB010773)
98. Moulik P, Ekström G. 2014 An anisotropic shear velocity model of the Earth's mantle using normal modes, body waves, surface waves and long-period waveforms. *Geophys. J. Int.* **199**, 1713–1738. (doi:10.1093/gji/ggu356)
99. Chang SJ, Ferreira A, Faccenda M. 2016 Upper- and mid-mantle interaction between the Samoan plume and the Tonga–Kermadec slabs. *Nat. Commun.* **7**, 10799. (doi:10.1038/ncomms10799)
100. Fichtner A, Trampert J. 2011 Resolution analysis in full waveform inversion. *Geophys. J. Int.* **187**, 1604–1624. (doi:10.1111/j.1365-246x.2011.05218.x)
101. Liu Q, Beller S, Lei W, Peter D, Tromp J. 2022 Pre-conditioned BFGS-based uncertainty quantification in elastic full-waveform inversion. *Geophys. J. Int.* **228**, 796–815. (doi:10.1093/gji/ggab375)

102. Freissler R, Schuberth BSA, Stotz IL, Zaroli C. 2025 Towards integrating tomographic resolution and uncertainty information into geodynamic mantle flow reconstructions. Figshare. (doi:10.6084/m9.figshare.c.8203613)
103. Oeser J, Bunge HP, Mohr M. 2006 Cluster design in the Earth Sciences—Tethys. *High Perform. Comput. Commun. Proc.* **4208**, 31–40. (doi:10.1007/11847366_4)
104. Crameri F, Shephard GE, Heron PJ. 2020 The misuse of colour in science communication. *Nat. Commun.* **11**, 5444. (doi:10.1038/s41467-020-19160-7)
105. Krischer L, Megies T, Barsch R, Beyreuther M, Lecocq T, Caudron C, Wassermann J. 2015 ObsPy: a bridge for seismology into the scientific Python ecosystem. *Comput. Sci. Discov.* **8**, 014003. (doi:10.1088/1749-4699/8/1/014003)